Draft

SC-LATV(09:1)4.1

Version: 29.06.2009

ASSOCIATION EURATOM - UNIVERSITY OF LATVIA

AEUL

ANNUAL REPORT 2008

Riga 2009

Edited by Dr. habil. phys. Olgerts Dumbrajs
Technical assistance by MSc.phys. Elina Laizane
Institute of Solid State Physics University of Latvia
8 Kengaraga Street, LV-1063, Riga, Latvia
Phone: +371 67 187 816
Fax: +371 67 132 778
E-mail: ISSP@cfi.lu.lv
Web: http://www.cfi.lv

TABLE OF CONTENT

1. INTRODUCTION

This Annual Report summarises the fusion research activities of the Latvian Research Unit of the Association EURATOM-University of Latvia in 2008.

The activities of the Research Unit are divided in the Fusion Physics Programme and Technology under the Contract of Association and Technology Programme under EFDA.

The Physics Programme is carried out at IP UL – Institute of Physics, University of Latvia, and at ISSP UL – Institute of Solid State Physics, University of Latvia. The research areas of the Physics Programme are:

- Preparation of a gallium jet limiter for testing under reactor relevant conditions
- Characterization of the impurity concentration, profiling and erosion in ITER relevant materials using laser ablation spectroscopy
- Theory and Code Development.

The Technology Programme is carried at ISSP UL and at ICP UL - Institute of Chemical Physics, University of Latvia. The technology research and development under EFDA is focused on:

- Determination of tritium and analysis of carbon-based plasma-facing components before and after their detritiation with different methods
- Effects of magnetic field, radiation and temperature on tritium release from the EXOTIC 8-3/13 neutron-irradiated beryllium pebbles

Several Staff Mobility actions took place in 2008: to IPP Garching, FZK Karlsruhe, UKAEA Culham, and ISTOK Lisbon.

2. FUSION PROGRAMME ORGANIZATION

2.1 Programme Objectives

The Latvian Fusion Programme, under the Association EURATOM-University of Latvia, is fully integrated into the European Programme, which has set the long-term aim of the joint creation of prototype reactors for power stations to meet the needs of society: operational safety, environmental compatibility and economic viability. The objectives of the Latvian programme are: (i) to carry out high-level scientific and technological research in the field of nuclear fusion, (ii) to make a valuable and visible contribution to the European Fusion Programme and to the international ITER Project in our focus areas. This can be achieved by close collaboration with other Associations.

2.2 Association EURATOM-University of Latvia

The Latvian contribution to the European fusion programme began in 2000 in the form of cost-sharing actions (fixed contribution contracts with EURATOM). The Association was established on 19 December 2001 incorporating the existing cost-sharing actions into its work plan.

2.3 Fusion Research Units

The Latvian Research Unit of the Association EURATOM-University of Latvia consists of three Institutes of University of Latvia.

1. IP UL – Institute of Physics, University of Latvia
   32 Miera St., Salaspils LV-2169, Latvia.
   Phone +371 6 7944700, Fax. +371 6 7901214
2. ISSP UL – Institute of Solid State Physics, University of Latvia
   8 Kengaraga St., Riga LV-1063, Latvia.
   Phone +371 6 7187810, Fax. +371 6 7132778
3. ICP UL - Institute of Chemical Physics, University of Latvia
   4 Kronvalda Blvd., Riga LV-1010, Latvia.
   Phone +371 6 7033884, Fax. +371 6 7033884

2.4 Association Steering Committee

The research activities of the Latvian Association EURATOM-University of Latvia are directed by the Steering Committee, which comprises the following members in 2008:

Mr. Douglas Bartlett, EU Commission, Fusion association agreements, Unit J4, DG Research
Mr. Steven Booth, Fusion association agreements, Unit J4, DG Research
Mr. Marc Pipeleers, Administration and finance, Unit J5, DG Research
Mrs. Maija Bundule, Ministry of Education and Science
Mr. Ivars Lacis, University of Latvia
Mr. Andrejs Silins, Latvian Academy of Sciences

The Steering Committee had one meeting in 2008, at ISSP UL with remote participation of EU Commission representatives, on July 10th.

2.5 The Latvian Members in the EU Fusion Committees

Consultative Committee for the EURATOM Specific Research and Training Programme in the Field of Nuclear Energy-Fusion (CCE-FU)
Mr. Andris Sternberg, ISSP UL

EFDA Steering Committee
Mr. Andris Sternberg, ISSP UL

Science and Technology Advisory Committee (STAC)
Mr. Olgerts Dumbrajs, ISSP UL
Mr. Andris Sternberg, ISSP UL
Governing Board for the Joint European Undertaking for ITER and the Development of Fusion Energy, "Fusion for Energy" (F4E GB)
Mrs. Maija Bundule, Latvian Academy of Sciences
Mr. Andris Sternberg, ISSP UL

EFDA Public Information Group

Mr. Maris Kundzins, ISSP UL

2.6 Public Information

Conferences

Results of fusion research were presented at:

- the annual scientific conference of University of Latvia,

Exhibitions

Educational activities

Television, press

Presentation in the TV programme “Science in Latvia”,
Presentation in the programme “Researchers’ Night in Latvia” on 26th of September, 2008.

2.7 Funding and Research Volume 2008

In 2008, the expenditure of the Association EURATOM-University of Latvia was about EUR, including Staff Mobility actions.

3. PHYSICS PROGRAMME – FUSION PHYSICS

The fusion physics work has been performed at two institutes in very close co-operation with other EURATOM Associations, in particular EURATOM-IST, Portugal, EURATOM-ENEA, Italy, EURATOM IPP, Germany, and EURATOM- FZK, Germany

.3.1. PREPARATION OF A GALLIUM JET LIMITER FOR TESTING UNDER REACTOR RELEVANT CONDITIONS

Principal investigators: ***E.Platacis***

ABSTRACT

In 2008 a paper [1] was published summarizing the results of the work with a liquid gallium jet limiter on the tokamak ISTTOK. These results can be characterized by a following citation from the abstract "… It was stated that ISTTOK has been successfully operated with the gallium jet without degradation of the discharge or a significant plasma contamination by liquid metal. This observation is supported by spectroscopic measurements showing that gallium radiation is limited to the region around the jet. Furthermore, the power deposited on the jet has been evaluated at different radial locations and its temperature increase estimated". An additional practical achievement should also be underlined - the fully new technology of preparation and introduction of liquid gallium in the vacuum of the discharge chamber was mastered. But ISTTOK is a typically small size tokamak {major radius R=0.46m, minor radius r=0.085 m, toroidal magnetic field B_t=0.45T, center electron temperature $T_e(0)$=150 eV, centre electron density $n_e(0)=5x10^{18}m^{-3}$, plasma current I_p~6kA, loop voltage V_p~3V}. It means that in the sense of all the critical to the process loads the mentioned results are giving not so much. To make a step towards more reactor relevant conditions in 2007 a collaboration agreement among three associations (ENEA, Frascati-IST, Lisbon – University of Latvia) on the development of liquid metal systems for protection of plasma facing components was signed. A high magnetic field, high plasma density, high current tokamak, the Frascati Tokamak Upgrade FTU {*R=0.93m, r = 0.28m, B=8T, I=1.6 MA*}, was chosen for potential next step experiments. On FTU, due to reduced dimension, the power per unit would be comparable even with that of ITER.

EXPERIMENTAL SETUP

On Fig.3.1.1a and 3.1.1b two schemes have been compared how such an experiment on FTU could look like. The geometry of ISTTOK practically allowed only for one version when the jet is introduced through the upper port and evacuated trough the opposite lower one. In principle such a directly downward directed jet could be incorporated also in the cross section of FTU. However, at such a version the clearance inside the design becomes very limited, no more than a few centimeters remain free from the jet to the outer wall and to the internal corner of the lower port, it is difficult to find a place free for installation of some additional units, etc.

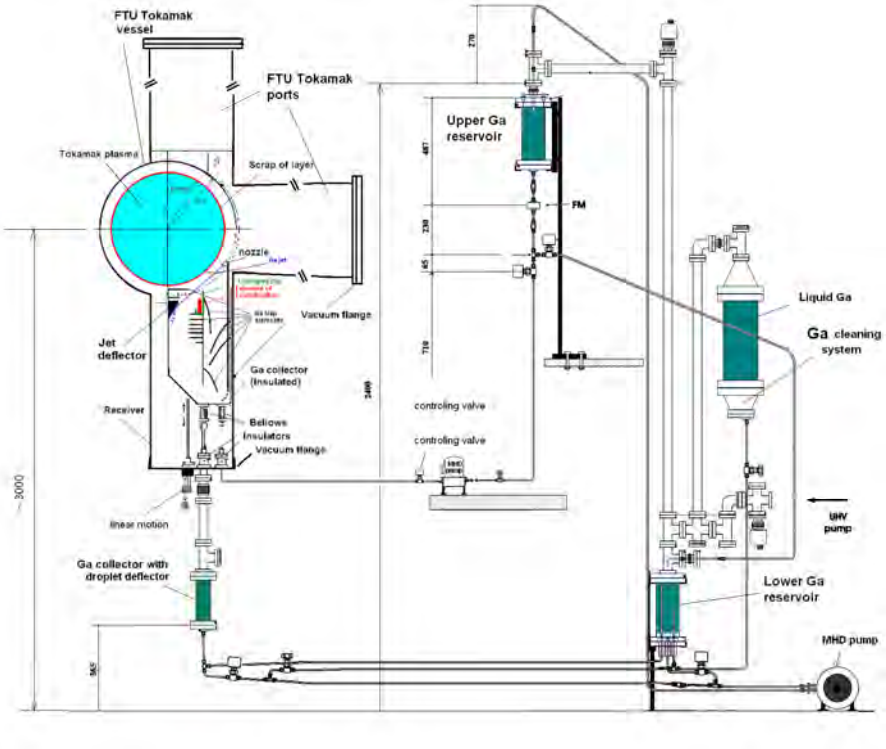

Figure 3.1.1.a

But the cross section of FTU allows also for other versions when the jet is touching upon the plasma under a definite angle and in the same time all the constructive elements remain placed outside the scrape-of layer. Under such conditions the jet must be backed by some droplet trapping sub-channel draining the liquid metal down into the main receiver installed in the lower port. It is essential since at the beginning and at the end of the approx. 5 s long jets “discharge” the mass of Ga will fall directly downwards. Additionally, it is necessary to give a definite space for some deflection of the jet by the plasma which was detected on ISTTOK. In the version Fig.1a the feeding channel is also installed trough the lower port. However, in such a case the feeding/receiving unit looks rather complicated, with very little clearance inside, with a necessity to come very close to the SOL. To ensure a gradual deepening of the jet into plasma a vertical

displacement of the nozzle must be foreseen. The corresponding mechanism also requires place. In the second version Fig.1b the feeding channel is installed through the side port. In such a case the outer hydraulic chain becomes more complicated, however, more clearance for all the components can be found. A horizontal displacement of the nozzle must be foreseen, the deepening can be started with a very low initial level. It can be seen on the figure that jets of the length L ~0.4m are needed, the loads are requiring the velocities on the level v~ 10m/s. Break-up in droplets remains as one of the tools for minimization of the MHD interaction, however, it requires a very exact relation between the velocity, length and diameter.

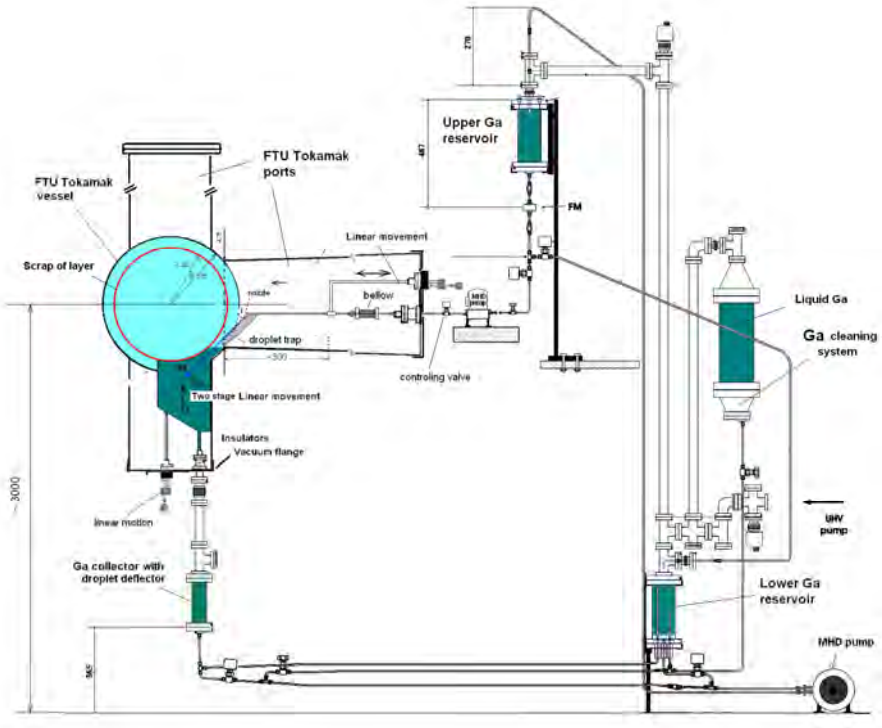

Figure 3.1.1.b

More flexible would be the version when the continuity of the jet would be broken by means of targeting it against a ceramic stopper. In any case, the geometry of the receiver should be investigated rather carefully, to avoid back-splashing etc. The possibility to transfer to a multi-jet version allowing to scrape-of already a real SOL should also be remembered.

For both the versions together with the cross sections of FTU schemes are given how the system could be joint to the feeding Ga stand. The hydraulic scheme of the gallium jet limiter on ISTTOK has been taken as a base. . It means that the main liquid metal technologies mastered on ISTTOK could be used also on FTU, that a definite number of design units could be directly transferred, that new in essence procedures and tools will not be needed.

STABILITY OF LONG LIQUID METAL JETS.

The working length of the jet L will always be roughly proportional to the small radius of the plasma. In the case of ISTTOK r = 85 mm and in the experiments the length of the jet was kept on the level L ~ 10cm. After a great number of measurements with different metals (Hg, InGaSn and Ga) a dimensionless dependence, characterizing the stability of the jet, was constructed: $L/d = 4.2\ Wb^{1/2}$, where L stays for the break-up length, d for the diameter of the jet and Wb for the Weber number. In the case of FTU r = 300mm, it means, the working lengths of the jet will be approx. equal to L ~ 35 cm. It can be checked also on Fig.1. It was not fully clear what will the behavior of a liquid metal jet at such high values of the relative length (L/d > 100). A corresponding experiment was performed on our Ga stand. In the test section a 50cm long glass cylinder was installed, instead of the previous model of ISTTOK's chamber (Fig.3.1.2.a,b). It was stated that the d = 3mm InGaSn jet remains stable over all the length of the cylinder.

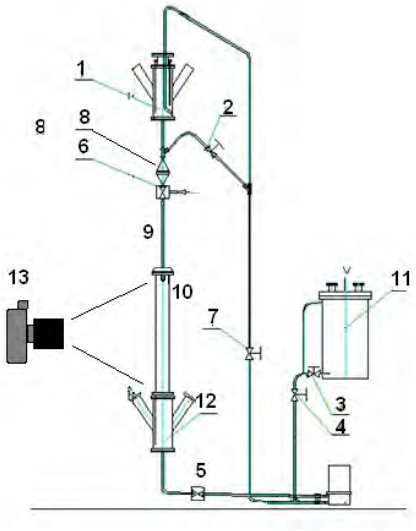

1-upper tank; 2-7-valves; 8-flow meter; 9-tube; 10-glass tube D45mm; 11-hot tank; 12-supply tank; 13-photo camera

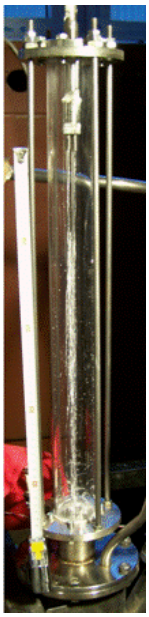

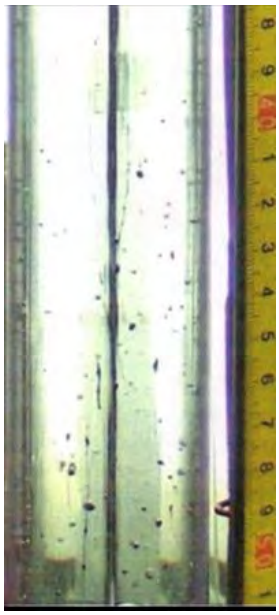

a b c

Figure 3.1.2.

As an example on Fig.3.1.2.c a photo of the length interval 30cm-40cm is presented. It should be underlined that also the break-up length of such long jets remains depending on the same mentioned above relation. A conclusion can be drawn that generation of long enough Ga jets should not cause essential problems. Additionally, to generate such long jets the equipment and methods tested on ISTTOK and at IPUL could be directly applied.

LIQUID METAL JETS IN STRONG MAGNETIC FIELDS.

The case of FTU specific are very high values of the main magnetic field, theoretically up to 8T.Therefore the question about the behavior of jets in strong fields remains topical, in spite of the fact that the general tendency was cleared already in the previous years - an orthogonal field enhances, and essentially, the stability of the jet. Basing on experiments with Hg and InGaSn jets in an up to 3.4 T field (electromagnet with permendure field concentrators) for the break-up length L a following empiric dependence was developed: $L/L_0 = 1+0.75Ha^{0.33}Re^{-0.25}$ where L_0 stays for the BUL without a field, Ha and Re for Hartman and Reynolds numbers. In a 5.6 T field the enhanced stability of a system of ten parallel InGaSn jets was demonstrated. In these previous experiments an ordinary N/He cooled superconducting magnet was used. Last year a modern cryogen-less superconducting magnet with 6T in a D=30cm and L=967cm bore was acquired, mainly for fusion related MHD investigations. In the very first set of experiments the stable behaviour of an InGaSn jet in high fields was demonstrated. Our many times used Incans stand was connected to the magnet by a parallel hydraulic arm adapted for proper feeding and draining of the test section.

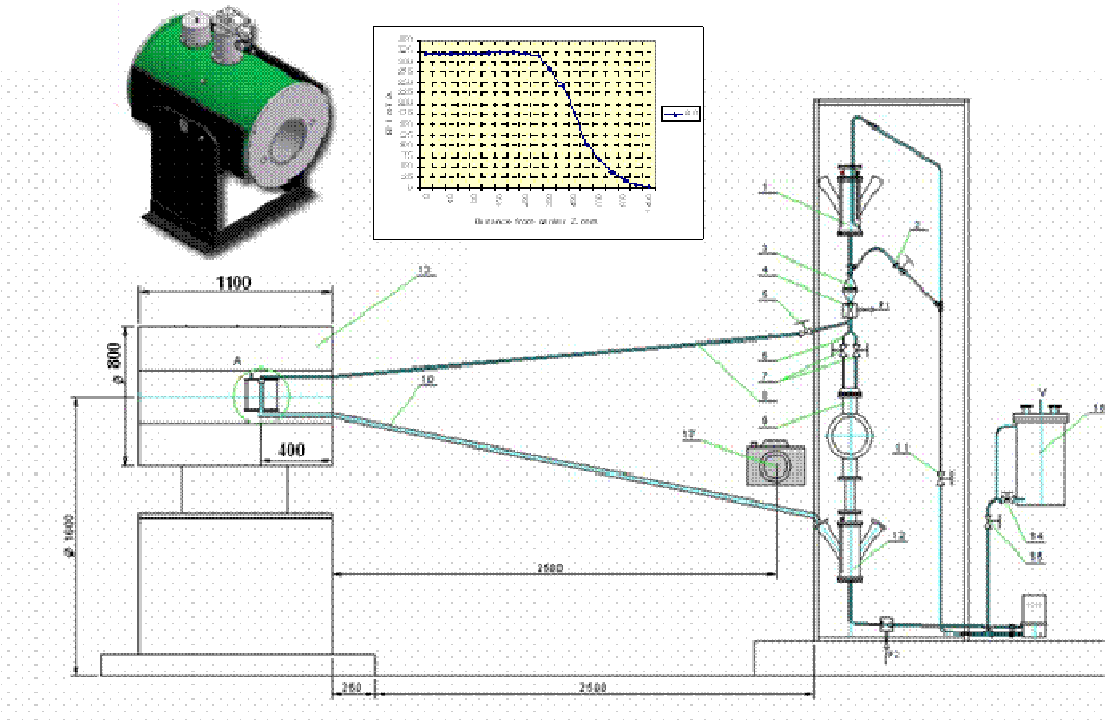

Figure 3.1.3.

The test section was based on a glass cylinder with a d=3mm nozzle in the centre of the upper lid (Fig.3.1.4.). In the lower lid an opening for draining was foreseen, rather simple by configuration, newer the less, working surprisingly well, especially in the presence of strong fields.

Without the field the behaviour of the liquid metal jet was familiar, typical to any liquid jet, with definite fluctuations, splashing, etc. Already in a 1T field the jet was like a string in view, without any remarkable by eye fluctuations and outlet splashing. This picture remained practically unchanged also at values of the field 2, 3, 4 and 5 T.

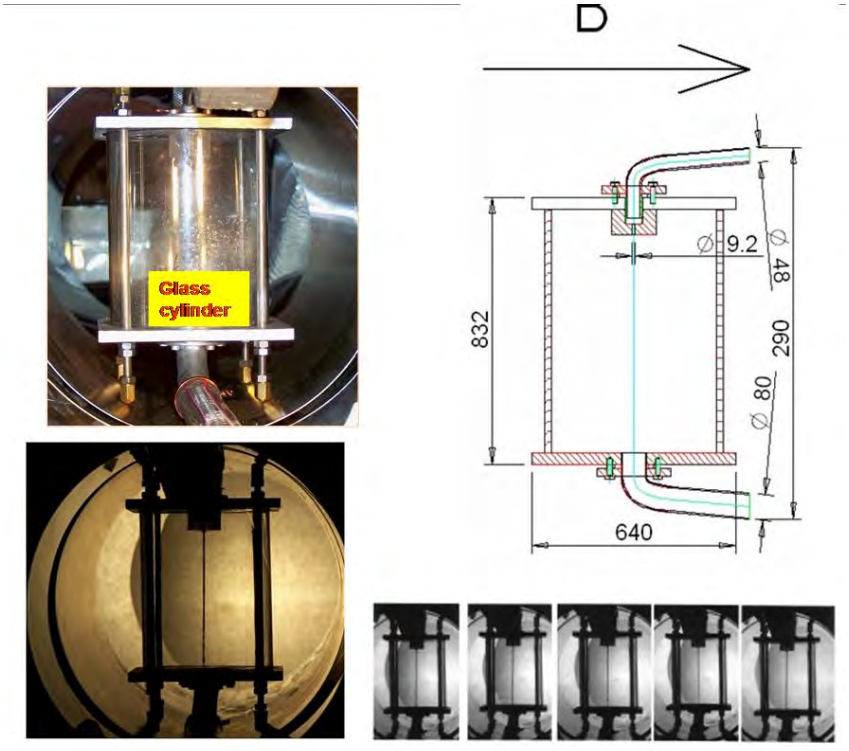

Figure 3.1.4.

3.1.1. SPECTROSCOPY OF LIQUID Ga JET VAPOURS IN THE REACTOR PLASMA

Principal investigator ***I. Tale***

UPGRADE OF THE EQUIPMENT FOR DETECTION OF THE INPURITY DISTRIBUTION AND DECAY KINETICS IN THE POLODIAL PLANE OF VESSEL.

A new design of the light accepting optics concerning modification of the optical fiber bundle has been provided. (Fig.3.1.1.1). It the early experiments only four fiber groups of possible seven were used to perform the scan in the poloidal plane of tokamak. This was due to the geometric magnification of the signal at the fiber bundle exit end. This problem was solved by a new fiber bundle, which also allows performing both the stationary and the time–resolved spectroscopic measurements of ISTTOK plasma. The entrance end of the fiber bundle consists of two rows total 2x15 fibers. One of the rows appearing at the exit end is devoted to the stationary spatially resolved measurements. The other 15 fibers are divided into three bundles having five fibers each ready to be coupled either to the monochromator of the interference filter. The separated the Ga line intensities are detected by three photomultiplier tubes. Afterwards the PMTs signal will be acquitted using digital storage oscilloscope. The time resolved signals from three different regions in the poloidal plane will be obtained.

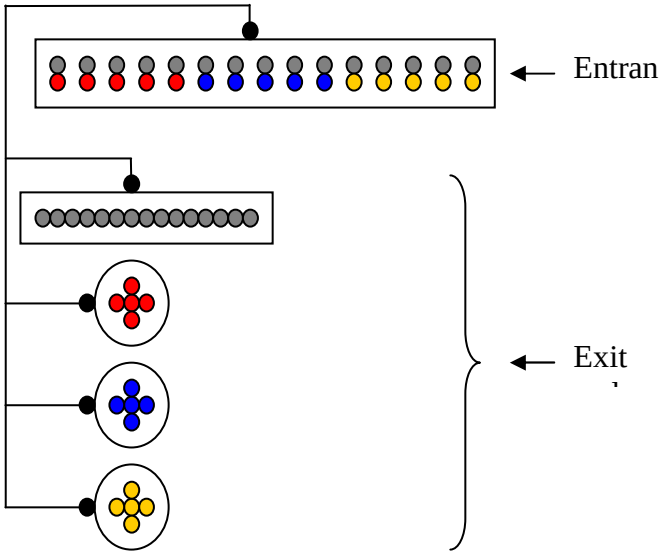

Figure 3.1.1.1. The fiber configuration in the bundle

At the entrance two fiber rows total 2x15 fibers collect the plasma emission.

At the exit end:

• Row 1 exit: the integrated spatially resolved emission spectra measurements using spectrograph and CCD camera.

• Row 2 exit: Time resolved spectroscopy from three different regions in the poloidal (or thorodial) plane. Three bundles each having five fibers over monochromator or interference filter are coupled to separate photomultiplier tubes. Multi channel digital storage oscilloscope is to be used for acquisition of the fluorescence decay with time resolution 1 ns.

The fiber bundle was fabricated at the Enterprise "Z-light Limited", Livani, Latvia.

Characteristics of the fiber bundle for simultaneous registration of the spatial distribution and average concentration of the impurities in plasma have been approved at the experimental setup for investigation of laser ablation plasma at ISSP (Fig.3.1.1.2).

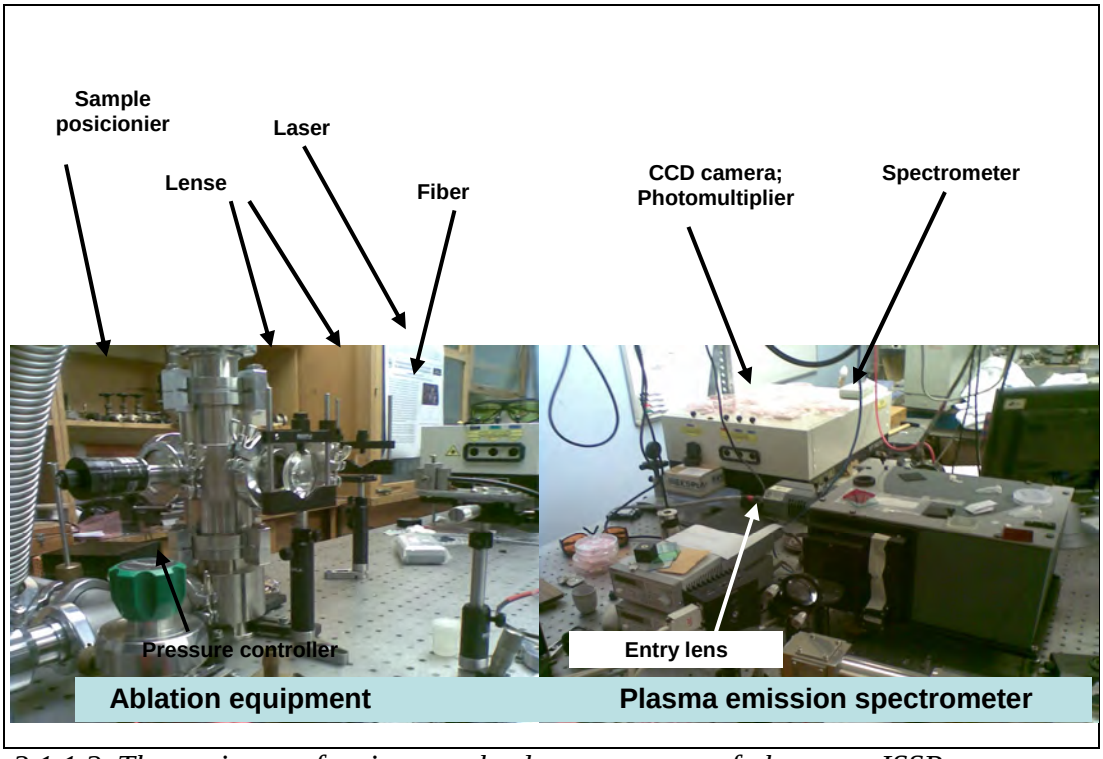

Figure 3.1.1.2. The equipment for time resolved spectroscopy of plasma at ISSP

Simultaneously can be registered:

• Plasma emission spectrum using ANDOR Shamrok sr-303 spectrogaph equipped with ANDOR type NEWTON CCD camera

• Decay kinetics of the single element line either at given one of four positions in the plasma plume or integral emission at four positions using TETRONIKS TDS 684A oscillograph equipped with fast photomultiplier type FEU-103 (Russia).

Fig.3.1.1.3 represents decay of C- line depending on the distance from surface of the carbon tile (ASDEX Upgrade tokamak).

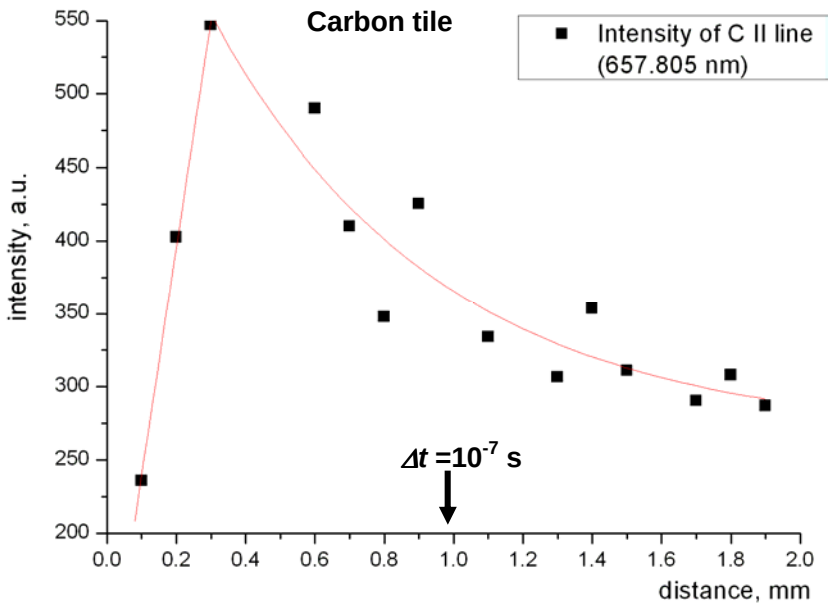

Figure 3.1.1.3 Decay of the C II line of carbon tile ASDEX upgrade

Results of the test experiments certificate that the upgraded plasma emission collection system is ready for time – resolved spectroscopy of Ga vapors at the tokamak ISTTOK Portugal.

Realization of the experiments planed during the 2008 due to the technical problems at ISTTOK in installation of the multi-jet liquid Ga source has been postponed to 2009.

DEVELOPMENT OF THE TECHNIUE FOR THE Ga VAPOR DISTRIBUTION WITH THE MULTIJET Ga JET AT THE TOKAMAK FTU FRASCATTI

Experience in spectroscopy of impurities in the tokamak plasma during investigations of the single liquid Ga jet provided at tokamak ISSTOK, Portugal has been used for design of experiments at tokamak Frascatti.

The design of optical fiber bundle developed for time resolved spectroscopy at ISSTOK is planed to use for experiments at Frascatti.

According to the construction of the horizontal port and present design of the multijet liquid Ga jet, proposed by the Institute of Physics UL the optical measurements only in the polodial plane are possible. Information of the vapour distribution before and after position of the Ga-jet is planed to obtain by linear changing of the position of the optical system lens-fiber bundle entry in thorodial direction.

Sketch of implementation of the system for measurements of plasma emission is shown in Figure 3.1.1.4.

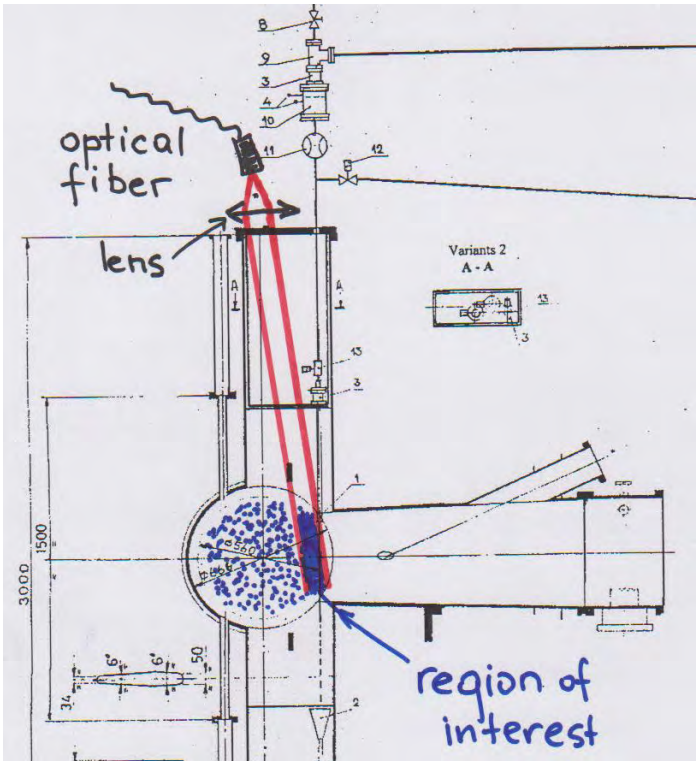

Figure 3.1.1.4. Design sketch of the plasma emission at the view port 1 of tokamak FTU Frascatti

CONCLUSION

The optical system (lens-optical fiber bundle) for time resolved core-exchange spectroscopy of impurities in the tokamak plasma has been developed.

Characteristics of the optical system are approved at Institute of Solid State physics UL.

The system is available for planned experiments at the tokamak ISSTOK and at the tokamak FTU Frascatti.

3.2. CHARACTERIZATION OF THE IMPURITY CONCENTRATION, PROFILING AND EROSION IN ITER RELEVANT MATERIALS USING LIBS

Principal investigator: ***I.Tale***

ABSTRACT

Several methods of analyzing the surface and impurity content in the near-surface layers are currently employed. An alternative method of establishing the impurity content in solid materials is laser-induced breakdown spectroscopy. This powerful tool for spectra-chemical analysis provides both impurity content analysis and layer-by-layer depth profiling. Here we present spectral information and discuss questions regarding the depth profiles of the impurities.

INTRODUCTION

Laser-induced breakdown can be defined as the generation of a practically totally ionized gas (plasma) by the end of the laser pulse. The interaction of a high-power laser pulse with a condensed phase target leads to a wide range of nonlinear phenomena. According to the simplified model, when the laser beam hits the surface of the solid sample, a portion of the incident light is transformed into heat energy, which raises the electrons to higher energy levels and transfers the energy to the surrounding surface by electron impact. This is followed by the eruption of material at high velocity and the formation a crater on a solid surface. The interaction mechanism between laser radiation and the matter depends on the parameters of the laser beam, such as wavelength, pulse rate and duration, as well as the chemical composition and physical properties of the target material.

In fusion devices, plasma-facing materials (PFMs) are bombarded and heated up to high temperature by high fluencies of energetic hydrogen ions and neutrals. This interaction causes erosion and penetration of impurity atoms into the plasma and subsequent deposition back onto the wall surfaces. Such impurities form layers with substantially different properties compared to those of the original material.

EXPERIMENTAL SETUP

A schematic diagram of the experimental setup for laser-induced ablation spectroscopy is shown in Fig. 3.2.1.

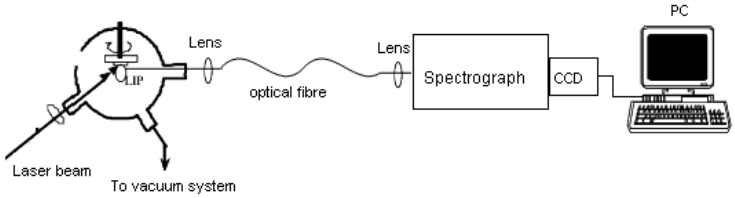

Figure3.2.1. Schematic of the experimental setup

As the laser-induced plasma source, a Q-switched Nd:YAG laser (SL-312, EKSPLA) with an emission wavelength of 1064 nm was used. It operates at a pulse repetition rate of 10 Hz, pulse width of 135 ps, and tuneable pulse energy up to 250 mJ. The diameter of the output laser beam is 1 cm. A convex quartz lens with a focal distance of 300 mm in the visible focused the beam at a distance of 3 mm inside the sample which was fixed on a rotating sample holder in the vacuum chamber. The vacuum system comprises of a turbomolecular pump (Ilmvac) and MicroPirani pressure sensor (MKS Instruments). The average energy of the laser beam was monitored by a power/energy meter (Ophir, model PE25BB-DIF). A quartz lens projected the plume image of the laser-induced plasma onto the entrance of the optical fibre which was placed in the image plane of the plume. The collected light was imaged via the fibre bundle onto the vertical slit of Andor Shamrock sr-303i spectrograph with a grating of 1200 gr/mm. The spectrograph was equipped with an Andor CCD camera. The depth of the craters was estimated by Dektak 150 Surface profiler (Veeco Instruments, Inc.).

The samples used in this study were cut from the graphite R6710 inner wall of the ASDEX Upgrade tokamak.

The laser beam was focused at a distance of 3 mm behind the sample surface in order to increase the diameter of the crater relative to its depth, and to avoid spark ignition in air. In case of slight defocusing of the beam, the ablation of the minimal amount of mass can be achieved (Fig.3.2.2.). If the focus of the laser beam is directly at the surface of the sample, the layer containing deuterium evaporates too quickly.

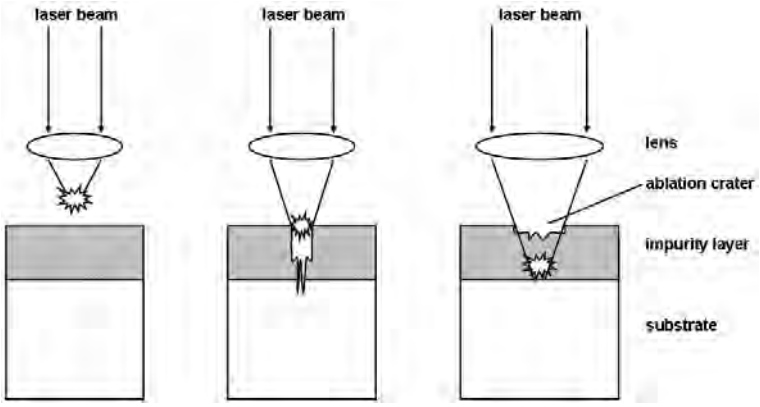

Figure 3.2.2. Laser beam focusing onto the sample

SAMPLES

Two types of samples were used: samples cut from the graphite R6710 divertor of the ASDEX Upgrade tokamak after a boronization process and graphite R6710 samples to provide a reference spectrum of carbon.

RESULTS

The experiments were carried out at three different pressures in a vacuum chamber, and at the atmospheric pressure. A sequence of 10 laser pulses of λ=1064 nm at the pulse energy of 25 mJ were applied on the targets. Obtained spectra are demonstrated in Fig.3.2.3. The legend on each series of laser-induced ablation spectra indicates the pressure value. For each pressure, 10 spectra were recorded, and 3 spectra were registered at the atmospheric pressure.

The spectra taken at the pressure value of 10^{-5} Torr is the richest in lines. As the pressure increases, the number of detected spectral lines diminishes. The spectra taken in the atmospheric pressure show the least amount of the spectral lines, but their relative intensities are increased almost twofold compared to those recorded at lower pressures. This may be explained with the models of propagation of laser-induced plasma plume demonstrating the development of high pressure region at the leading edge of the plume. At atmospheric pressure, laser-induced plasma is confined at the region next to the surface of the ablated material. The front edge of the ablation plume interacts with the background gas species, resulting in elevated brightness of the plume in the imaging point.

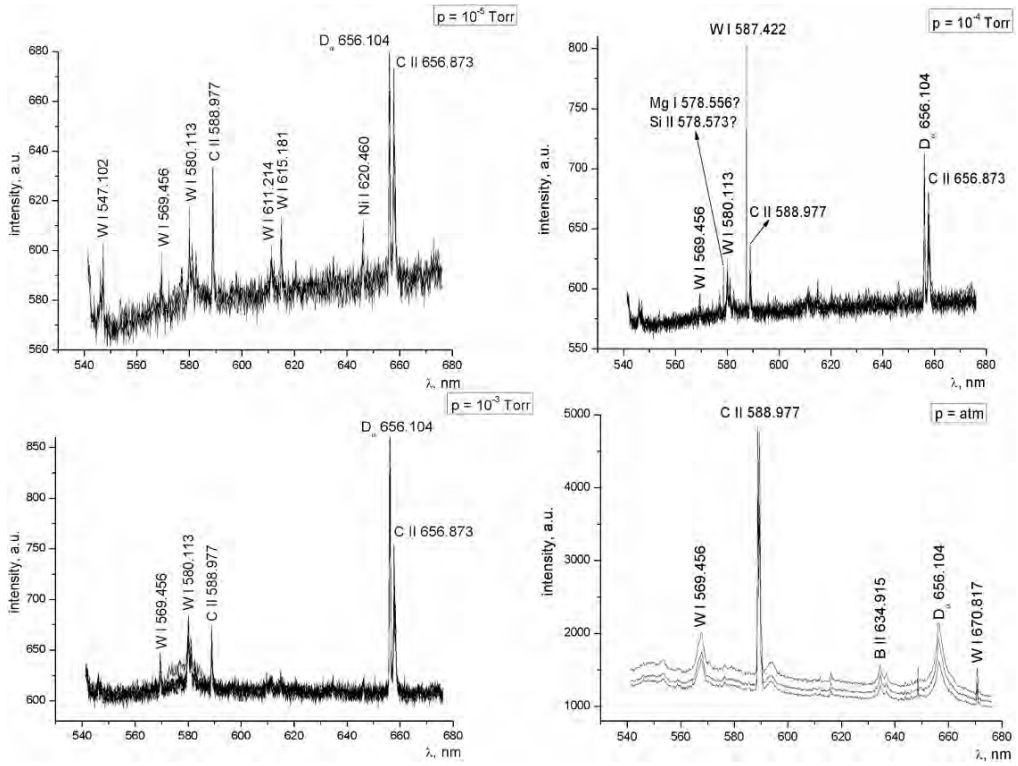

Figure 3.2.3. Line spectra of different elements measured at different gas pressure for ASDEX Upgrade tiles R6710 after boronization.

This leads to increasing of the relative intensity of spectral lines observed at atmospheric pressure. It has also been shown that lower background pressure results in a lower laser energy threshold for ablation. That is why the spectra of the sample in atmospheric pressure taken under otherwise same conditions demonstrate smaller amount of detected spectral lines comparing to the rest of the spectra in the Fig. 3.2.3.

To record laser-induced plasma emission spectra, 10 laser pulses of energy of 10 mJ were applied on the both samples. Both of the spectra are represented in Fig.3.2.4. The spectrum of a graphite sample containing no impurities was recorded as the reference. The spectrum of the ASDEX Upgrade sample shows a substantial number of impurities. Tungsten lines are detected. The reason for the appearance of B II (345.130 nm, 634.927 nm) lines might be a process of boronization of plasma-facing components (surface conditioning). Fe I 390.294 nm and Ni IV 444.519 nm might come from the stainless steel components which are not shielded from the plasma.

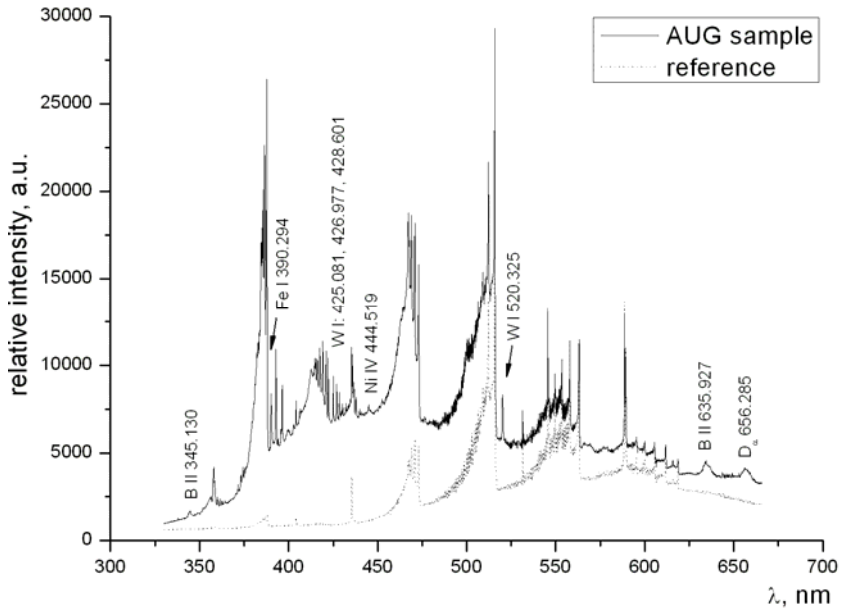

Figure 3.2.4. Laser-induced plasma emission spectra of graphite R7610 reference and ASDEX Upgrade sample. Carbon lines are not specified on the figure

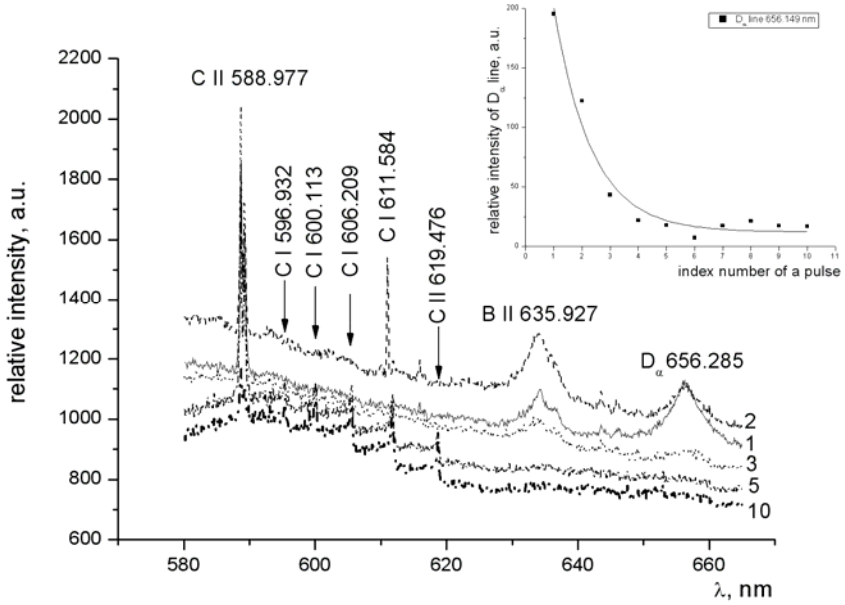

Figure 3.2.5. Appearance of D_α 656.285 nm line in the laser ablation spectrum of ASDEX Upgrade sample. The numbers on the right side correspond to the index number of the pulse in the sequence. The inset shows the decay of D_α 656.285 nm line intensity.

Although both of the spectra were recorded under the same conditions, the relative intensities of the spectral lines belonging to the reference sample are considerably lower than those of the ASDEX Upgrade sample. This might be due to surface differences in the ablated samples. Reference graphite R7610 sample was polished smoothly in contrast to the ASDEX Upgrade

sample, which is much rougher and demonstrates the traces of erosion after the plasma discharge. Also, the ablation rate differs substantially for these samples. For ASDEX Upgrade sample the average material removal rate was about 0.5 μm per single laser pulse. However, for pure graphite sample this value was close to 70 nm. This is in agreement with the fact that target reflectance determines the amount of laser pulse power absorbed by the material. Additionally, surface defects are of great importance as they contribute to decreasing the laser intensity threshold required to initiate vaporization of the surface.

Weak D_α 656.285 nm line has also been detected in the ASDEX Upgrade sample. To follow the evolution of the appearance of deuterium line in the spectrum, signals in the spectral window of 580-680 nm were recorded. Fig.3.2.5. represents spectra corresponding to the 1st, the 2nd, the 3rd, the 5th and the 10th consecutive laser pulses applied at the same spot of the sample. The signal was recorded after each pulse.

D_α line appears after the 1st laser pulse. Afterwards, the decrease of deuterium signal in comparison with the carbon line is observed. D_α line has nearly vanished after applying the 2nd laser pulse. The inset demonstrates that by the end of the series of laser treatment the intensity of D_α line has decreased almost two-fold compared to that after the 1st pulse. After a sharp decreasing of the intensity of deuterium line, the signal becomes practically equal to the background level. This happens as the impurity layer on the ASDEX Upgrade target is removed by the ablation process. The layer could be as thick as (3 ÷ 4) × material removal rate, which is around 0.5 μm per laser pulse (Fig.3.2.6.).

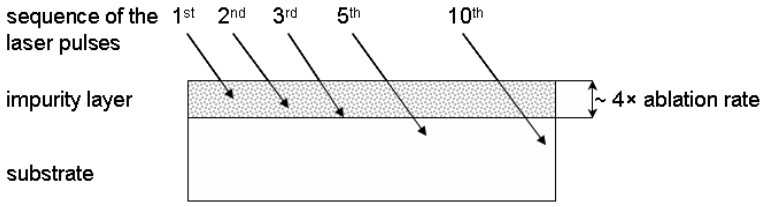

Figure 3.2.6. Process of the ablation of impurities in ASDEX Upgrade target.

When the laser pulse interacts with the target surface, the elements of the impurities appear in the spectrum. In the beginning of the ablation process, the intensities of the spectral lines of deuterium and boron are higher than those of the carbon. The relative intensities of spectral lines corresponding to the impurities and carbon change drastically when the number of laser pulses applied to the same spot increases. The signal of the substrate of the ASDEX Upgrade target remains consistent or increased. The first pulses show only the most intense CII 588.977 nm line, while the other C I-II lines start to appear after the end of the 5th pulse.

These observations are in agreement with the models and experimental results of laser-induced plasma plume propagation. In atmospheric pressure, the plasma is constrained to small volumes close to the target surface. As the forces sustaining the high pressure region of the plume dissipate, the propagation decelerates and the front edge relaxes. This leads to a portion of plume material being deposited back on the target surface. More volatile elements will condense out of the cooling plasma later than more refractory phases. This condensed material presents a source of the refractory element enriched material which is sampled at the later stages of ablation.

CONCLUSION

Qualitative elemental analysis of ASDEX inner wall tiles was performed by laser-induced plasma spectroscopy. The main advantages of this method are: its simplicity, its ability to simultaneously monitor all elements in plasma, that no sample preparation is required, and that it is able to analyse any material, irrespective of its physical state. The thickness of the ablated layer in the case of the PFM was around 0.5 μm per laser pulse, but for the polished reference sample about 70 nm. The spectra show a decrease of deuterium signal and an increasing signal of the substrate during the layer-by-layer ablation process. These results show that laser-induced breakdown spectroscopy is a potential method of analysis of migrating materials and co-deposited layers of PFMs. The quantitative characteristics of this effect will be the subject of further investigations. Additionally, laser scanning can be used as a procedure of deuterium removal from co-deposited layers.

3.3 THEORY AND CODE DEVELOPMENT

3.3.1 HYSTERESIS IN MODE COMPETITION IN HIGH POWER 170 GHZ GYROTRON FOR ITER

Principal investigator ***O.Dumbrajs***.

ABSTRACT

Hysteresis in mode competition in high power *170GHz* gyrotrons for ITER is studied. Specific examples of hysteresis with respect to variation of magnetic field, current, electron beam radius and beam voltage are given.

INTRODUCTION

Gyrotrons are microwave sources whose operation is based on the stimulated cyclotron radiation of electrons oscillating in a static magnetic field. Gyrotron devices are now able to generate several orders of magnitude as much power at millimeter wavelength as classical microwave tubes, and can operate at frequencies higher than are conveniently available from other types of tubes. Gyrotron oscillators can have a wide application, including technological processes, atmospheric sensing, ozone conservation, artificial ionospheric mirror, extra-high resolution electron spin resonance spectroscopy, nuclear magnetic resonance spectroscopy, new medical technology spectroscopy, etc. However, the main application of powerful gyrotrons is electron cyclotron resonance plasma heating in tokamaks and stellarators and the noninductive current drive in tokamaks.

The study of one very interesting phenomenon – hysteresis - is relatively limited, although perfect understanding of hysteresis is important in connection with mode competition, frequency tuning, voltage overshooting, amplitude modulation of the signal, etc. In gyrotrons hysteresis is the phenomenon that causes the amplitude of oscillations to lag behind the magnetic field and the voltage, so that operation regions of modes for rising and falling magnetic field and voltage are not the same.

In the present work, we generalize our single mode hysteresis calculations to multimode case with particular emphasis on mode competition in *170GHz* gyrotrons for ITER. The theory is illustrated by a number of specific examples.

FORMALISM

Theoretically hysteresis can be studied most conveniently using a time-dependent equation for the oscillation amplitude. In such calculations the equation is solved for a given fixed value of the parameter of interest until the onset of stationary oscillations. After this, this parameter is increased by a small amount and calculations are continued until again the onset of stationary oscillations. This is repeated until the desired parameter value is reached. Next such calculations are carried out in the reverse direction with decreasing parameter values.

SPECIFIC EXAMPLES

For a better understanding of various hysteresis phenomena, let us consider two specific modes: the operating $TE_{34,10}$ mode at frequency *170.00GHz* and the parasitic $TE_{34,10}$ mode at frequency *167.25GHz*.

HYSTERESIS WITH RESPECT TO MAGNETIC FIELD.

Oscillation regions for these modes are shown in figure 3.3.1.1.

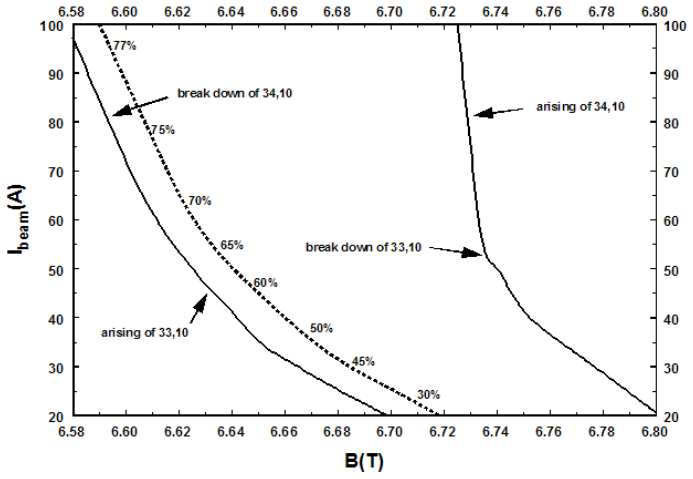

Figure 3.3.1.1. Oscillating regions of the operating (34,10) and parasitic (34,10) modes. Here U_b=65kV and α=1,24

Suppose that the operating current is *I=45A.* It is seen that for this current the maximum efficiency $\eta_{\perp} \approx 60\%$ is at the magnetic field $B \approx 6.65T$. However, due to the "wall" created by the parasitic $TE_{33,10}$ mode one cannot approach this point from the low field side. One has to start at

$B \approx 6.75T$ and decrease the field to $B \approx 6.65T$. The corresponding hysteresis loop is shown in Fig.3.3.1.2.

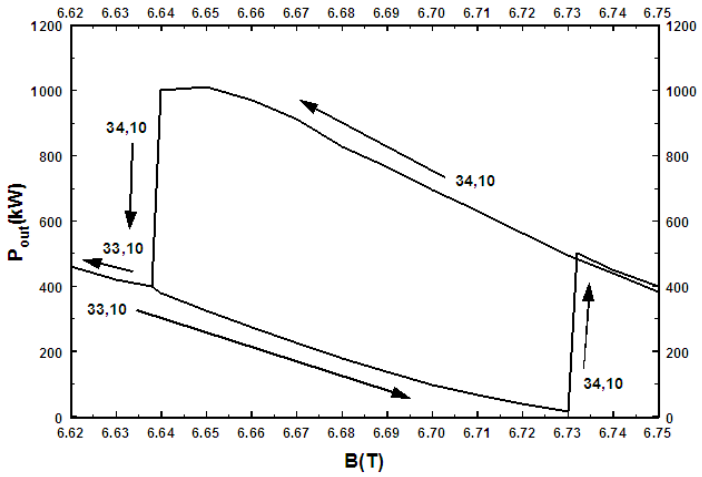

Figure 3.3.1.2. Hysteresis loop for the operating $TE_{34,10}$ *and parasitic* $TE_{33,10}$ *modes*

It is seen that at $B = 6.75T$ (starting point) the gyrotron oscillates in the operating mode with the output power $400\,kW$. By reducing the magnetic field to $B = 6.65T$ it is possible to obtain the maximum output power of about *1000kW*. Further reduction of the magnetic field to $B = 6.64T$ leads to the switch over to the parasitic mode with low output power. The power in the parasitic mode can be increased by further decreasing of the magnetic field. However, if we want to regain high power oscillations in the operating mode, we have to increase the magnetic field down to $B = 6.73T$, where oscillations return to the operating mode and the hysteresis loop is closed.

It is remarkable that precisely such a scenario and a similar hysteresis loop have been observed in the recent experiment with $TE_{31,8}$ as an operating mode and $TE_{30,8}$ as a parasitic mode.

HYSTERESIS WITH RESPECT TO BEAM VOLTAGE.

Let us discuss hysteresis with respect to the beam voltage. This effect can be easily observed also in gyrotrons with diode guns. We keep again the magnetic field fixed $B = 6.65T$ and change the beam voltage. The corresponding hysteresis loop is shown in Fig. 3.3.1.3.

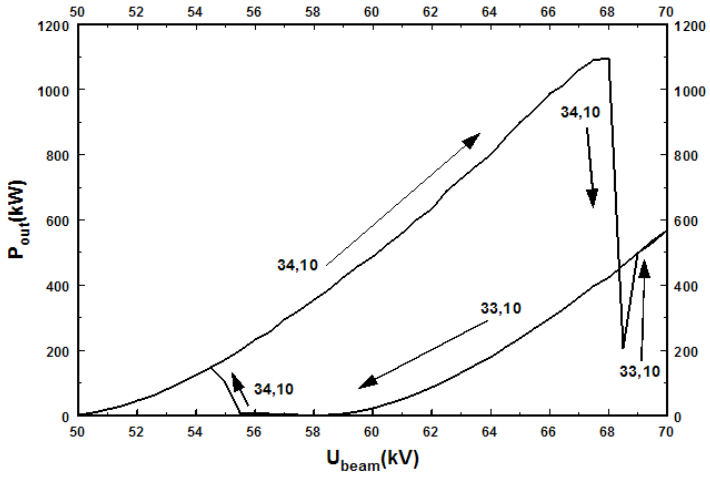

Figure3.3.1.3. Hysteresis loop with respect to the beam voltage

By raising during the start-up the voltage to about *68 kV* we reach the optimal operating point with output power about $1100\,kW$. However, due to hysteresis we have to be absolutely sure that no large "oscillations" in the voltage occur, due to imperfections of the power supply. Indeed, overshooting over $68\,kV$ will lead to the loss of operating mode and to oscillations in the parasitic mode with low output power. Oscillations in the operating mode can be recovered only at about $55\,kV$ with low output power. At this point one can resume climbing up the hill to high voltages and output power. The described picture means also that in gyrotrons with power modulation due to hysteresis one has to be cautious with overshooting.

CONCLUSIONS

Various hysteresis manifestations in the competition between the operating $TE_{m,p}$ and parasitic $TE_{m-1,p}$ modes have been explored. Specific examples have been given for the operating $TE_{34,10}$ and parasitic $TE_{33,10}$ modes in the high power $170\,GHz$ gyrotron for ITER.

3.3.2. LINEAR AND NON-LINEAR INSERTS FOR GENUINELY WIDEBAND CONTINUOUS FREQUENCY TUNABLE COAXIAL GYROTRON CAVITIES

Principal investigator ***O.Dumbrajs***

ABSTRACT

We consider two continuous frequency tunable CW coaxial gyrotron oscillators, one 330 GHz with 3 GHz bandwidth and output power 50 – 400 W for scientific applications and one 30 GHz with 0.4 GHz bandwidth and output power 40 – 140 kW for industrial applications. The continuous tuning of both gyrotrons is achieved by moving the linearly tapered inner conductor in the axial direction in combination with the proper adjustment of the operating magnetic field. We consider also a non-linear tapering, which makes it possible to reduce the length of the insert and to improve efficiency of the device.

INTRODUCTION

Frequency step-tunable gyrotrons for Electron Cyclotron Resonance Heating (ECRH) of magnetically confined fusion plasmas and for Electron Cyclotron Current Drive (ECCD) in plasmas were considered already earlier.. In recent years, new exciting applications of gyrotrons have emerged beyond fusion plasma applications. For example, Dynamic Nuclear Polarization (DNP) to enhance signal to noise ratio in Nuclear Magnetic Resonance (NMR) and Electron Spin Resonance (ESR) spectroscopy experiments as well as material processing in the industry. In all these applications, the possibility of tuning the gyrotron frequency is a great advantage.

There are several possibilities to change the frequency of a gyrotron oscillator by changing: i) the accelerating and modulation voltages (electrical tuning), ii) the magnetic field (magnetic tuning) and iii) the physical dimensions of the oscillator using a split cavity structure or a movable piston (mechanical tuning). Recently, an operation in the higher order axial modes was proposed for a smooth variation of frequency within a particular axial mode and between adjacent axial modes. It should be emphasized that as long as the cavity geometry is not changed during the operation, the tuning is possible only in discrete steps, which are determined by the difference between the eigenvalues of the modes. The exception is the so-called frequency pulling by changing the electron beam parameters while keeping the oscillating mode. However, the latter method has no practical applications, because the bandwidth is inversely proportional to the diffractive quality factor of the cavity, and thus is extremely small.

Coaxial cavity gyrotrons open new possibilities in tuning the frequency in a truly continuous way. This is achieved by moving a tapered inner conductor in the axial direction. We apply this

method in a 330 GHz gyrotron useful for NMR experiments and in a 30 GHz one for industrial applications. In addition, we examine the possibility to decrease the length of the insert and to keep the output power almost constant by means of a non-linearly tapered inner conductor.

LINEARLY TAPERED INSERT

Fig. 3.3.2.1. shows a coaxial gyrotron cavity with a linearly tapered insert that is movable along the longitudinal axis. By moving the conical insert to the left the outer to inner radii ratio $C = R_{cav,0}/R_{in,0}$ decreases, leading to a relevant change to the resonance frequency f_0 and the diffractive quality factor Q_{diff}, which strongly depends not only on the radii ratio, but also on the slope of insert.

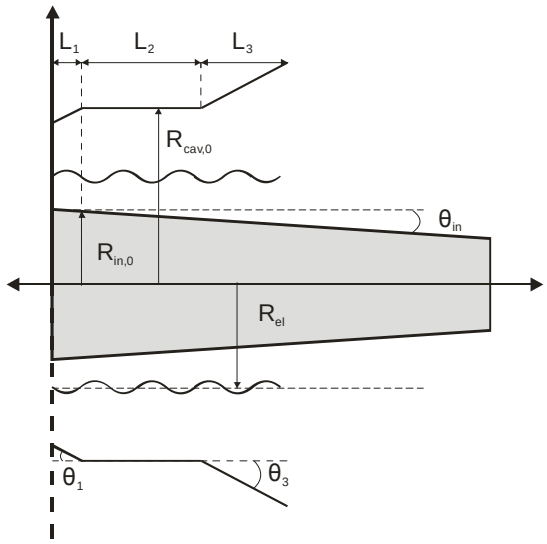

Figure 3.3.2.1. The geometry of a coaxial cavity with an axially movable tapered insert

THE 330 GHZ GYROTRON FOR NMR EXPERIMENTS

A 330 GHz step frequency tunable gyrotron with the operating mode $TE_{+6,2}$ has a conventional cavity and its resonance frequency varies by fixed values that are determined by the distance of the axial $TE_{6,2,n}$ modes. Here, we consider a similar coaxial cavity with the geometrical details given in the first column of Table 3.3.2.1. Table 3.3.2.2. presents the dependence of the frequency and the quality factor on the axial displacement of the insert (positive displacement values correspond to the movement of the insert to the left). Here as the cavity geometry changes, the magnetic field is readjusted to remain in resonance with the given mode and to maintain the optimum coupling between the electron beam and the RF field.

Table 3.3.2.1. Geometrical characteristic of the cavity with the linear insert

Geometrical Parameter	330 GHz gyrotron for NMR applications
$R_{cav,0}$	1.62 mm
$R_{in,0}$	0.961 mm
L_1	2.73 mm
L_2	11 mm
L_3	8 mm
θ_1	3°
θ_2	3°
θ_{in}	-0.1°
R_{el}	1.2 mm

Table 3.3.2.2. Resonance frequencies and quality factors for the 330 GHz cavity with the linear insert.

Shift (mm)	f_0 (GHz)	Q_{diff}
0	332.880	1382
5	332.166	1543
10	331.539	1742
15	331.008	1986
20	330.560	2287
25	330.200	2660
30	329.914	3126
35	329.707	3696

It is evident that for the maximum shift of 35mm (value being chosen arbitrary) the frequency decreases by 3.173 GHz. Since the quality factor of the cavity is high in the whole tuning range, one can expect high efficiencies at all frequencies. Indeed, the calculations with the operating parameters V=20 kV, I=50 mA, pitch factor α=2 and R_{el}=1.2 mm, confirm this and predict high output power for the whole tuning range, as shown in Fig. 3.3.2.2. It should be emphasized that the results presented in this figure have been obtained with a fixed operating current 50 mA. With larger currents it should be possible to maintain constant output power in the entire tuning range. It should be noted that the proposed tuning is genuinely continuous. The tuning range is limited by the length of the insert and by the mechanical feasibility of the proposed design, which should be

optimized for any specific inverted Magnetron Injection Gun (MIG), whose emitter is fixed, but the coaxial insert movable.

It is important to mention that mode competition is deliberately ignored in our study, since the spacing between the neighbouring low-order modes is large enough to neglect this problem.

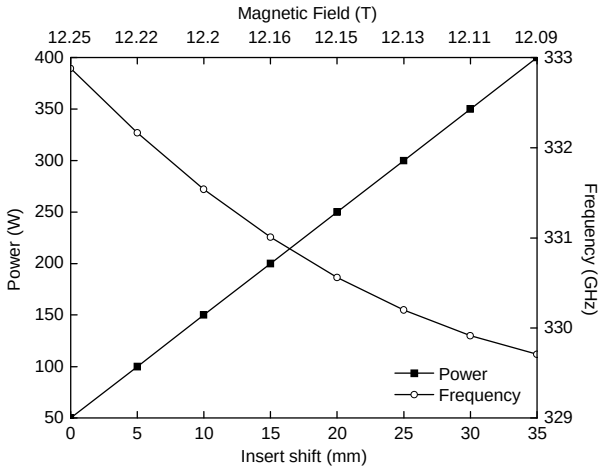

Figure 3.3.2.2. Dependence of the frequency, the output power and the optimal magnetic field on the axial shift of the linear inner conductor for the 330 GHz gyrotron

NON-LINEARLY TAPERED INSERT

The realization of a cavity with a movable insert, such as those presented in the previous section, could be constrained by the length of the insert. A possible solution to this problem is the use of a non-linear tapering profile, for which the movement to the left will result in a combined change of the radii ratio and the tapering slope. Searching for a tapering profile that is almost linear at its beginning, we selected the following family of curves

$$R_{in}(z) = R_0\sqrt{1-\left(z / S_{\max}\right)^{\nu}}$$

where R_0 is the radius of the insert at position z = 0 mm and $S_{\max}$ and ν are parameters regulating the slope of the tapering.

Keeping intact the outer wall of the 330 GHz gyrotron cavity, we replaced the linear insert with a non-linear one with the geometric parameters R_0 = 0.973 mm, S_{max} = 200 mm and ν = 1. Cold cavity calculations presented in Table *3.3.2.3* show that with this insert it is possible to achieve the previous 3 GHz bandwidth with the shift of 20 mm, which corresponds to a 43% length reduction of the inner conductor. Unfortunately the quality factors now are smaller than in the case

of a linear insert. As a consequence, the beam current has to be increased in order to maintain the output power constant (Fig. 3.3.2.3.).

Table 3.3.2.3. Resonance frequencies and quality factors for the 330 GHz cavity with the non-linear insert with R_0 = 0.973 mm, S_{max} = 200 mm and ν = 1.

Shift (mm)	f_0 (GHz)	Q_{diff}
0	332.878	975
5	331.892	1146
10	331.083	1393
15	330.448	1760
20	329.980	2327

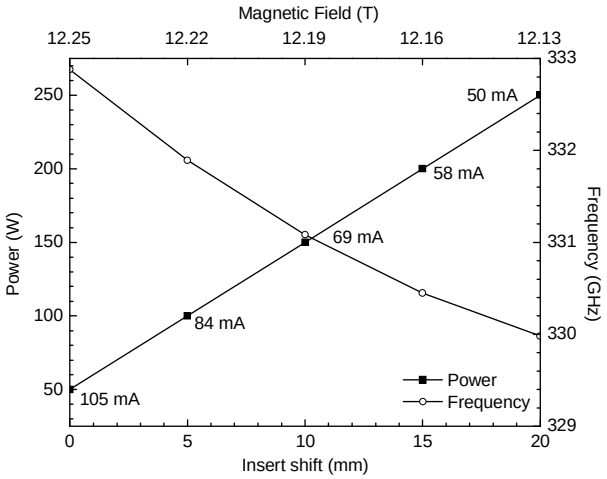

Figure 3.3.2.3. *Dependence of the frequency, the output power and the optimal magnetic field on the axial shift of the non-linear inner conductor for the 330 GHz gyrotron with R_0 = 0.973 mm, S_{max} = 200 mm and ν = 1*

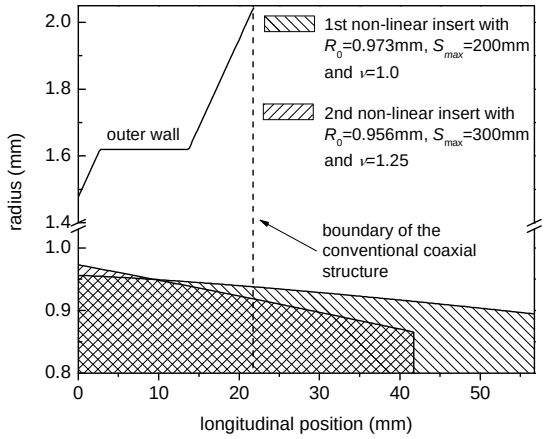

Figure 3.3.2.4. Representation of the two movable non-linear inserts proposed

In the previous case the inner conductor is slightly non-linear (Fig. 3.3.2.4.) and as a matter of fact we could obtain quite similar results by increasing the slope of the linear insert and by balancing the decrease of the length of the insert to decrease to the efficiency. However, it is possible to benefit much more from the non-linear tapering in another way. Consider the previous cavity with tapering parameters $R_0 = 0.956$ mm, $S_{max} = 300$ mm and $\nu = 1.25$. It is obvious from Table 3.3.2.4. that the quality factor of this cavity is of the same order for all shifts and one can expect to obtain almost constant efficiency in the whole frequency range, which is not very different from the previous cases. Fig. 3.3.2.5.which shows the dependence of the frequency, the output power and the optimal magnetic field on the axial shift of the insert confirms this expectation.

Table 3.3.2.4. Resonance frequencies and quality factors for the 330 GHz cavity with the non-linear insert with $R_0 = 0.956$ mm, $S_{max} = 300$ mm and $\nu = 1.25$.

Shift (mm)	f_0 (GHz)	Q_{diff}
0	332.894	2478
5	332.513	2379
10	332.123	2358
15	331.736	2387
20	331.364	2456
25	331.012	2562
30	330.688	2706
35	330.395	2892

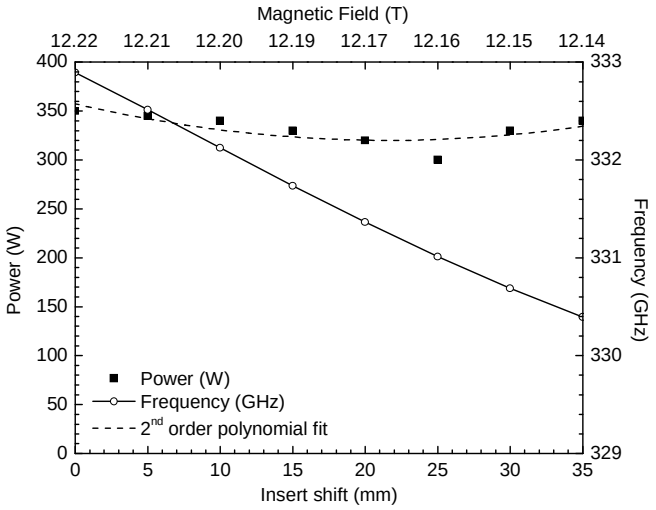

Figure 3.3.2.5. Dependence of the frequency, the output power and the optimal magnetic field on the axial shift of the non-linear inner conductor for the 330 GHz gyrotron with R_0 = 0.956 mm, S_{max} = 300 mm and ν = 1.25.

ALIGNMENT AND OHMIC LOSSES

The dimensions and weight of the proposed inner conductors are rather small, close to a size and weight of a needle. This should make easy to resolve alignment problems in specific practical mechanical designs of the cavity. On the other hand, this smallness can cause some difficulties related to overheating of the insert. For the 330 GHz gyrotron, where the predicted output power does not exceed 40 - 400 W, estimates show that the density of Ohmic losses at the insert surface ρ_i are not larger than 0.05 – 0.5 kW/cm^2. This should make it possible to operate the gyrotron in long pulse and CW regimes.

CONCLUSIONS

The genuinely continuous tuning of coaxial gyrotrons by moving the tapered inner conductor in the axial direction and by adjusting the operating magnetic field has been demonstrated for two cases. In both cases, the efficiency remains high in the whole frequency range and it is possible to retain constant the output power by increasing the beam current properly. The length of the inner conductor can be significantly shortened by increasing the slope of the tapering or by using a non-linear profile. The latter option provides better possibilities to keep the output power almost constant over the entire tuning range.

3.3.3. HYSTERESIS IN SAWTOOTH CRASH IN ASDEX UPGRADE TOKAMAK

Principal investigator ***O.Dumbrajs***

ABSTRACT

A hysteresis model is used to describe experimental data on sawtooth crash in theASDEX Upgrade tokamak. The model is based on hysteresis which arises due to the fact that the value of the current density gradient (approximated for the H-mode discharges studied here, by the temperature gradient) at the $q=1$ surface required to turn on the instability is greater than the gradient required to maintain the instability, once it is turned on. The value of the hysteresis parameter can be chosen such that the model reproduces correctly the two time scales of the sawtooth crash in the ASDEX Upgrade tokamak: the slow rise time (~7 *ms*) and the rapid crash time (~50 μs).

INTRODUCTION

Under a wide range of operating conditions tokamaks are subject to a relaxation oscillation in the centre of the plasma. This appears as a sawtooth oscillation of the temperature and density and is also observed on other plasma parameters. During the stable ramp phase heating raises the temperature and at the collapse the associated thermal energy is released to the outer part of the plasma in the form of a heat pulse. Usually it is assumed that the collapse is due to an instability which has an $m=1,\ n=1$ structure and is associated with the existence of a $q=1$ surface in the plasma. The sawtooth oscillations usually start when a $q=1$ surface first appears. The q profile also oscillates with a sawtooth-like behavior. During the ramp phase the current density around the axis increases and at the collapse it is reduced. Correspondingly the central value of q falls during the ramp and rises at the collapse.

In spite of the huge amount of both the experimental and the theoretical work devoted to studying of this phenomenon, sawtooth oscillations are far from being completely understood.

Recently we investigated non-complete sawtooth reconnection in the ASEDEX Upgrade tokamak. Such reconnection phenomena are associated with internal $m/n=1/1$ kink mode which does not vanish after the crash phase (as would be the case for complete reconnection). It was shown that this sawtooth can not be fully described by pure $m/n=1/1$ mode and that higher harmonics play an important role during the sawtooth crash phase. Here the Hamiltonian formalism was employed to reconstruct perturbations to model incomplete sawtooth reconnection. It was demonstrated that stochastization appears due to excitation of low- order resonances which are

present in the corresponding q profiles inside the $q=1$ surface which reflects the key role of the q_0 value. Depending on this value two completely different situations are possible for one and the same mode perturbations: (i) the resonant surfaces are present in q profile leading to stochasticity and sawtooth crash ($q_0 \approx 0.7 \pm 0.1$); (ii) the resonant surfaces are not present which means no stochasticity in the system and no crash event ($q_0 \approx 0.9 \pm 0.05$). Accordingly central safety factor value is always less than unity in case of non-complete sawtooth reconnection. With such a stochastic model we could well describe experimental observations. Next we derived heat diffusion coefficient in a stochastic magnetic field and solved the nonstationary diffusion equation which allowed us to study time evolution of sawtooth crash in ASDEX Upgrade.

In this paper we demonstrate that different timescales in a natural manner can be explained by means of the hysteresis phenomenon. We use the hysteresis model based on the transport catastrophe. In that model the sawtooth is shown to be independent of the growth of the $m=1$ mode and is related to a catastrophic bifurcation of the anomalous transport coefficient. The magnetic component in fluctuation increases as the plasma pressure increases. If the pressure gradient exceeds a certain threshold, a magnetic stochasticity sets in and the thermal conductivity is enhanced. The increment of the transport associated with the strong magnetic perturbation continues until the pressure profile is flattened. Hysteresis behaviour of transport flux to the pressure gradient is obtained. The current profile is influenced by the enhanced current diffusivity from the same mechanism, but the change in the q profile remains small. We use experimentally inferred values for the heat conductivity in the ramp up and the crash phase to model the experimentally observed time scales.

THEORETICAL MODEL

To describe experimental data on sawtooth crash in ASDEX Upgrade we adopt the model which has been used for studying avalanches in continuum driven dissipative systems. The model is based on the following system of equations:

$$\frac{\partial T(r,t)}{\partial t} = \chi(t)\frac{\partial^2 T(r,t)}{\partial r^2} + S(r) \qquad (1a)$$

$$\frac{\partial \chi(t)}{\partial t} = \frac{Q(|\partial T/\partial r|) - \chi(t)}{\tau} \qquad (1b)$$

$$Q(|\partial T/\partial r|) = \begin{cases} \chi_{\min}, & \textit{low state}, \quad |\partial T/\partial r| < \beta k \\ \chi_{\max}, & \textit{high state} \quad |\partial T/\partial r| > k \end{cases} \tag{1c}$$

Here $T(r,t)$ is the temperature, $\chi(t)$ is the diffusion term, $S(t)$ is the source term, and $\chi_{\max} >> \chi_{\min}$. The function Q is double valued and dependent upon the history for $\beta k < |\partial T/\partial r| < k$, where k is the instability threshold and $0 < \beta < 1$. The value of Q remains in the low state $Q = \chi_{\min}$ until the slope $|\partial T/\partial r| > k$, whereupon it undergoes a transition to the high state. However, when in the high state, $Q = \chi_{\max}$, it will not make the transition to the low state until the slope $|\partial T/\partial r| < \beta k$. Thus Q acts very much like a physical instability in that the value of the slope k required to turn on the instability is greater than the slope βk required to maintain the instability once it is turned on (*hysteresis!*). When Q changes to $\chi_{\max}$, a magnetic stochasticity sets in and the diffusive term $\chi(t)$ begins to rise toward $\chi_{\max}$.

It should be noted that our model employs the most simple heat conduction equation (1a). This is justified because we wish to study only different time scales in the sawtooth crash disassociating from accompanying changes of plasma parameters.

ASDEX UPGRADE SAWTOOTH DATA

The experimental temperature profile at ASDEX Upgrade before the sawtooth crash (#20975, t=4.13s) can be parameterized as follows:

$$T(r/a) = 2.46 \cdot \left(1 - \left(\frac{r}{a}\right)^2\right)^{1.3} \tag{2}$$

Here $a = 0.5\,m$ is the minor radius of the plasma. The $q = 1$ surface is located at $r/a = 0.3$. This allows us to determine the instability threshold in Eq. (1c): $k = 3.6\,keV/m$. Analyzing sawtooth crash in ASDEX Upgrade by means of the ordinary diffusion equation we found in Ref. 8 that $\chi_{\min} \approx 1 m^2/s$ and $\chi_{\max} \approx 2500\,m^2/s$ and that during the crash time $\tau \approx 40 \mu s$ the central temperature drops to $2.18\,keV$.

For the source term we choose the following form:

$$S(r/a) = S_0\left(1 - \frac{r/a}{0.3}\right), r/a \le 0.3 \tag{3}$$

which means that it increases the slope $|\partial T/\partial r|$ linearly.

As a result we have two free parameters in the system of equations (1a-1c): the strength of the source S_0 and the hysteresis parameter β. By changing these two parameters we can try to reproduce the experimental number for the full cycle of the sawtooth crash in ASDEX Upgrade which is about 7*ms*.

CALCULATIONS

We impose the Neumann boundary condition at the plasma interior:

$$\left.\frac{\partial T}{\partial r}\right|_{r=0} = 0 \tag{4}$$

and the Dirichlet boundary condition

$$T\left(\frac{r}{a} = 0.30, t\right) = 2.18\ keV \tag{5}$$

at the position of the $q = 1$ surface.

We start the calculations at the moment when the crash is completed, i.e., the temperature profile is flat ($T = 2.18\ keV$) and the diffusion coefficient is maximal ($\chi = \chi_{\max}$).

The results of the calculations with (3), $S_0 = 240\ keV/s$ and $\beta = 0.50$ are shown in Figs. 3.3.3.1.-3.3.3.6. In Figs. 3.3.3.1 and 3.3.3.2 one can see characteristic time scales for the instability. The rise time of the temperature is about 0.007 *s* (Fig. 3.3.3.1), while the crash time is about 0.00005 *s* (Fig. 3.3.3.2). In other words, the central temperature (Fig. 3.3.3.3.) rises from 2.18 *keV* up to 2.55 *keV* in about 7 *ms*, but drops from 2.55 *keV* to 2.18 *keV* in about 50 μs. This is related to the behavior of the diffusion coefficient as illustrated in Figs. 3.3.3.4 and 3.3.3.5. It appears "suddenly" after about 7 *ms* (Fig. 3.3.3.4) and decays to zero in about 150 μs (Fig. 3.3.3.5).

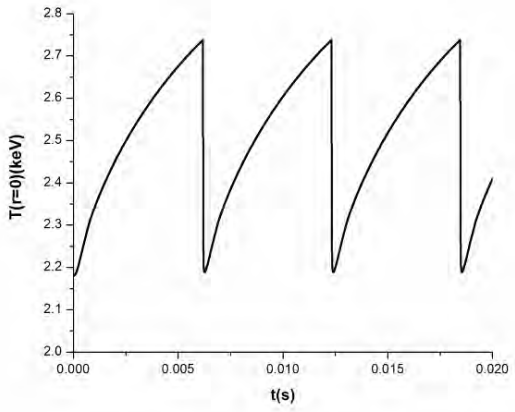

Figure 3.3.3.1. The periodic crash and build-up time of the central temperature are demonstrated

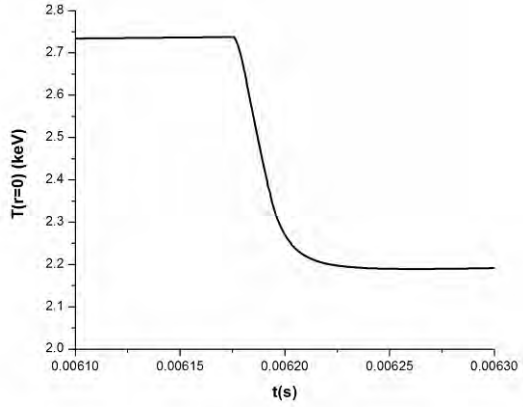

Figure 3.3.3.2. Temporal dependence of the central temperature in the vicinity of the first peak in Fig. 3.3.3.1.

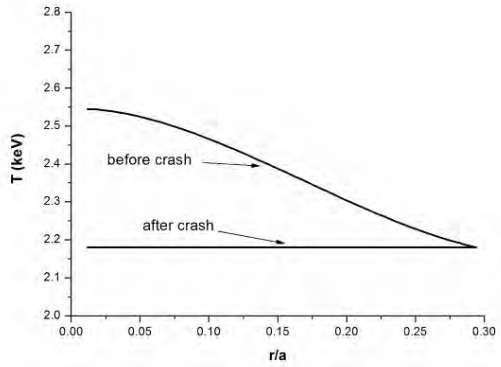

Figure 3.3.3.3. Temperature profile before and after the crash

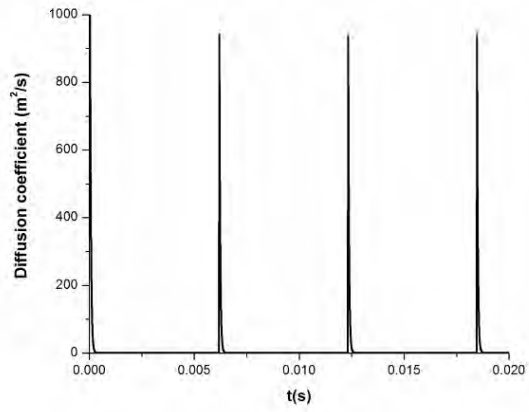

Figure 3.3.3.4. Temporal evolution of the diffusion coefficient

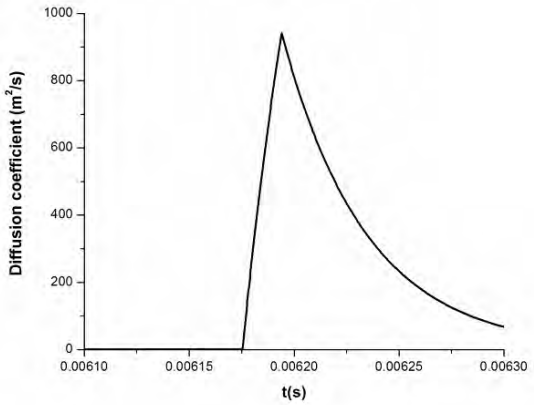

Figure 3.3.3.5. Temporal dependence of the diffusion coefficient in the vicinity of the first peak

In Fig. 3.3.3.6 we illustrate the hysteresis phenomenon as described by the model corresponding to Eq. (1).

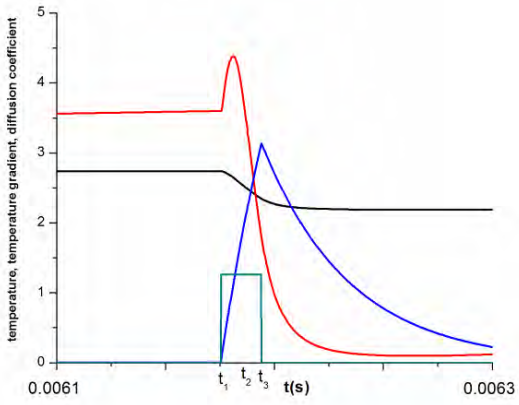

Figure. 3.3.3.*6. Hysteresis in sawtooth crash.Temperature gradient (red curve) rises until the instability threshold at* $3.6\,keV/m$. *At this moment* $t = t_1$ *the instability is turned on by switching the function* Q *(green curve, arbitrary units) to* $\chi_{\max}$. *The central temperature (black curve) begins to decrease and diffusion coefficient (blue curve, arbitrary units) begins to increase. During further evolution due to hysteresis the function* Q *is switched back to* $\chi_{\min}$ *not at* $t = t_2$ *when temperature gradient passes again the instability threshold, but at* $t = t_3$ *when temperature gradient becomes equal to* $\beta k = 1.8\,keV/m$

By changing the values of the parameters S_0 and β it is possible to regulate the width and the height of sawtooth peaks. Here larger S_0 values shorten the sawtooth period, but larger β values prolong it.

The form and the strength of the source term can be different in different experiments. We have chosen it as (3) only for illustrative purposes. If the source term is taken from experiment, then our model contains only one free parameter β. After fitting it so that Fig. 1 correctly reproduces experimental observations ($\beta = 0.5$), we can claim that during the crash the temperature gradient at the $q = 1$ surface in ASDEX Upgrade drops from $3.6\, keV/m$ to zero. This is a subject of experimental verification.

CONCLUSIONS

A hysteresis model has been used to describe experimental data on sawtooth crash in ASDEX Upgrade . It is based on hysteresis which arises due to the fact that the value of the temperature gradient at the $q = 1$ surface required to turn on the instability is greater than the temperature gradient required to maintain the instability once it is turned on. The value of the hysteresis parameter β and the source term have been chosen such that the model reproduces correctly the two time scales of the sawtooth crash in ASDEX Upgrade : the slow rise time (~7 *ms*) and the rapid crash time (~50 μs).

In further studies one should analyze other ASDEX Upgrade discharges, as well as sawtooth discharges in other tokamaks, by means of the proposed model in order to determine “universality” of β and S_0 and to understand the physical nature of β.

3.3.4. RADIATION STABILITY OF REACTOR MATERIALS

Principal investigator ***E.Kotomin***

OBJECTIVES

The experimental studies of novel materials for fabrication of radiation resistant materials for nuclear reactors suggested for study of oxide-dispersion strengthened steels (ODS) as reduced activation ferritic-martensitic structural materials for prospective fusion reactors. Reduced activation steels strengthened by yttria precipitates are considered as promising structural materials for future fusion- and advanced fission-reactors. In particular, application of oxide dispersion strengthened (ODS) steels for fusion reactor blanket structure allows increasing its operation temperature by ~100°C. Both size and spatial distributions of oxide precipitates significantly affect mechanical properties and radiation resistance of ODS steels. However, the mechanism of ODS nanoparticle formation is still not well understood. The aim of our theoretical study has been to continue the first principles modeling of ODS steels accompanied by kinetic Monte-Carlo simulations, in order to clarify a growth mechanism of ODS nanoparticles and conditions of their stability inside the *fcc* iron lattice.

INTRODUCTION

Some recent experiments indicate that at least part of yttrium oxide particles might be dissolved in the steel matrix during mechanical alloying. If so, yttrium dissolved above its equilibrium solubility limit will precipitate during hot isostatic pressing of mechanically alloyed powder. Slow diffusion of large substitutional yttrium atoms is probably a limiting factor for yttrium oxide particle growth. Diffusion of interstitial oxygen is much faster and, therefore, cannot delay the growth w Y-vacancy pair as a simplest diffusing yttrium-containing complex. In our model iron matrix is represented by a face-centered cubic γ-Fe lattice, which is stable at typical hot isostatic pressing temperatures. We have performed a series of large-scale first principles calculations on perfect γ-Fe lattice as well as that containing a single Fe atom vacancy, O and Y impurity atoms. Our calculations have shown that there is a considerable binding between yttrium atom and vacancy at some distances. This allows us to determine the pair-wise energies necessary for further kinetic Monte Carlo simulations, aimed at understanding the yttrium oxide precipitation process.

RESULTS

VASP-4.6 computer code with a plane-wave basis set has been used for large-scale first-principles calculations on both perfect and defective *fcc* lattice of high-temperature γ-Fe phase. The Perdew-Wang-91 GGA (Generalized Gradient Approximation) non-local exchange-correlation functional and the scalar relativistic PAW (Projector-Augmented Wave) pseudopotentials have been used for these calculations performed in parallel regime with a total geometry optimization. The pseudopotentials describe the core electrons of Fe ($4s^1 3d^7$ outer shell), O ($2s^2 2p^4$) and Y ($4s^2 4p^6 5s^1 4d^2$) atoms with 8, 6 and 11 external electrons, respectively. Magnetic effects were not taken into account since a cubic γ-Fe is known to be paramagnetic in the temperature range of its stability as mentioned above.

A series of preliminary calculations has been performed to define the parameters of the calculations reproducing the experimental data. This includes an analysis how the convergence of the results depends on the supercell size, the cut-off energy and the *k*-point set of the corresponding Brillouin zone. We have found that the calculations of the commonly used 27 atom 3×3×3 supercell are still inaccurate, due to a small size of the supercell which causes the noticeable elastic interactions between defects and its periodical image. Thus, the supercell has been extended to 64 atoms with the 4×4×4 dimensions. For the calculations on the yttrium atom pair inside the iron lattice, even larger, at least 4×4×6 (96-atom) supercell is required with a lower symmetry as compared to 4×4×4 structural unit. The cut-off energy has been varied from 300 to 1200 eV and the *k*-point set from 64 (4×4×4) to 4096 (16×16×16). It has been found that the results are reliably converged only beginning with the unusually large cut-off energy of 800 eV *vs.* default cut-off energy of 267 eV, while varying the *k*-point set, it has been found that at least 12×12×12 mesh allows us to obtain plausible results.

We have calculated key parameters of the atomic and electronic structure: The equilibrium lattice constant and cohesive energy for cubic paramagnetic γ-Fe lattice have been calculated to be 3.44 Å and 4.96 eV/atom, respectively. The energy of vacancy formation for 4×4×4 supercell has been found to be 2.37 eV with 0.75% inward relaxation. Our calculations performed for the 4×4×4 γ-Fe supercell have shown that oxygen atoms reside on either *O* (six nearest Fe neighbors) or *T* (four nearest Fe neighbors) interstitial positions (the latter has been found to be ~0.1-0.2 eV less favorable than the former). Y impurity atom can only substitute Fe atom in its vacancy (in the center of cuboctahedron formed by the nearest twelve Fe atoms) serving as a donor of electronic density (~1 *e*). At the next step, the interaction of 2 Y substitutional atoms at different inter-

distances (1-NN, 2-NN, 3-NN and 4-NN) has been calculated. Fig. 3.3.4.1. shows the model of Fe *fcc* supercell containing the two Y substitutes at the first nearest neighbors (1NN) positions.

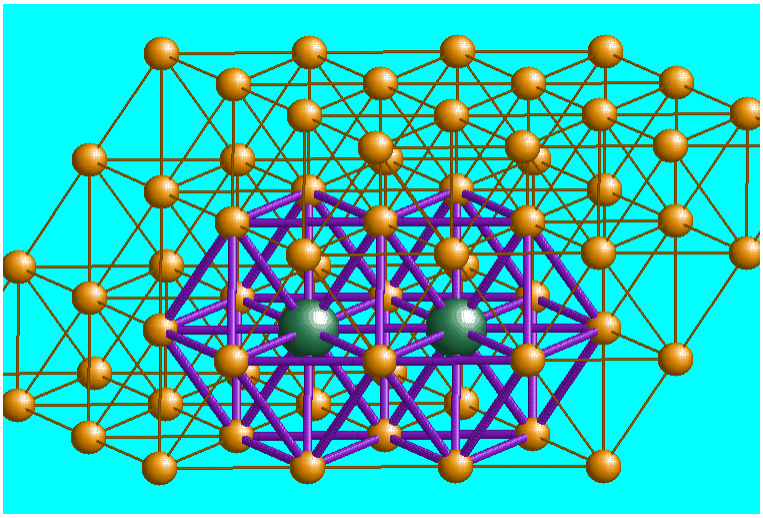

Figure. 3.3.4.1. 4×4×4 supercell of face-centered-cubic (Fm3m) structure of γ-Fe containing 2 Y substitute atoms in the 1NN positions

The binding energies between the two Y substitutes were calculated for all aforementioned configurations. Our calculations have clearly showed that no bonding exist between the two Y atoms inside the *fcc* Fe lattice. The results discussed are presented in Table 3.3.4.1.

Table 3.3.4.1. Formation and binding energies (E_f and E_b) calculated for the fcc Fe 4×4×4 supercell containing two Y substitute atoms at different inter-distances.

Configuration	4×4×4 supercell	
	E_f(eV)	E_b(eV)
Y-Y 1-NN	1.72	-0.73
Y-Y 2-NN	1.43	-0.45
Y-Y 3-NN	1.44	-0.46
Y-Y 4-NN	2.03	-1.05

$$E_{bY-Y} = E_{fY-Y} - 2E_{fY} \quad (1a)$$

$$E_{fY} = E_{confY} - \frac{N-1}{N}E_{conf\,id} - E_{cohY} \quad (1b)$$

$$E_{fY-Y} = E_{confY-Y} - \frac{N-2}{N}E_{conf\,id} - E_{cohY} \quad (1c)$$

where N is the number of atoms in the supercell, $E_{conf\,id}$ the total energy of the calculated ideal configuration, E_{cohY} the cohesive energy of Y, E_{fY} and E_{fY-Y} the formation energies of one and two Y atoms in the Fe lattice, respectively, $E_{conf\,Y}$ and $E_{conf\,Y-Y}$ the total energies of the calculated supercell with one or two Y substitutes, respectively, and E_{bY-Y} the binding energy of the two Y atoms in the γ-Fe lattice.

Then the interaction of Y substitutional atom and Fe vacancy at different interdistances has been calculated. The configurations of Y - Fe vacancy pair in the 1-NN positions before and after the relaxation are shown in Figs. 3.3.4.2.a, 3.3.4.2.b respectively.

a) b)

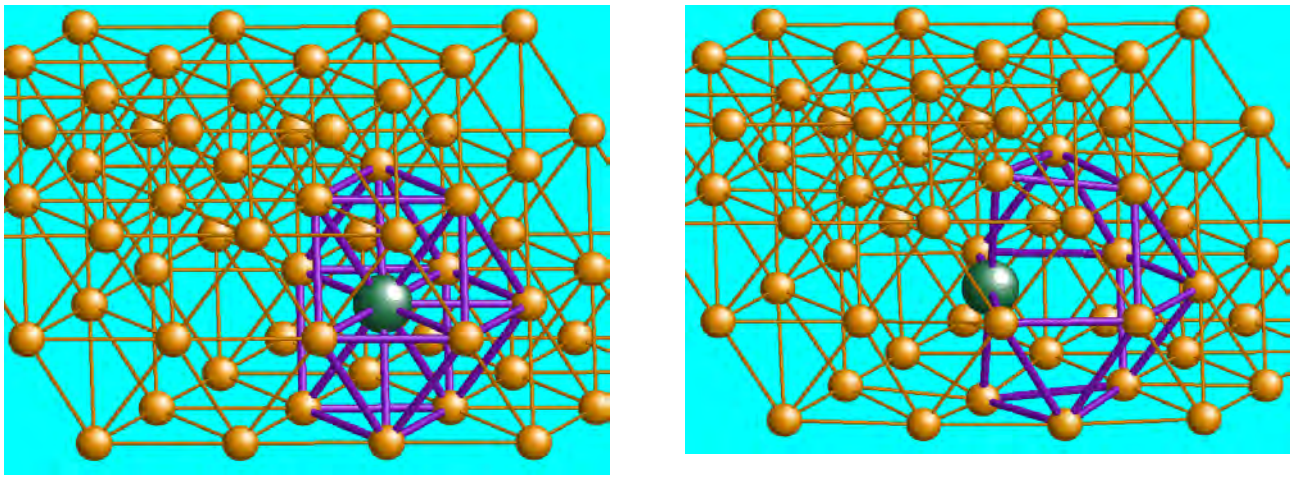

Figure. 3.3.4.2. a) 1-NN configuration of the Y-Fe vacancy pair in the Fe fcc lattice before the relaxation, b) 1-NN configuration of the Y-Fe vacancy pair in the Fe fcc lattice after the relaxation

The results of these calculations are presented in Table *3.3.4.2.* which clearly shows that inside the *fcc* lattice attraction between the Y atom and Fe vacancy occurs at 1-NN and 3-NN distances, *i.e.*, the bonding is expected to be found for the 1-NN, 3-NN and 4-NN configurations while the repelling is observed for 2-NN configuration.

Table *3.3.4.2. Formation and binding energies (E_f and E_b) calculated for the fcc Fe 4×4×4 supercell containing the Y substitute atom and Fe vacancy at different mutual distances.*

Configuration	4×4×4 supercell	
	E_f(eV)	E_b(eV)
Y-Fe vac. 1-NN	1.19	1.67

Y-Fe vac. 2-NN	3.07	-0.21
Y-Fe vac. 3-NN	2.57	0.30
Y-Fe vac. 4-NN	2.47	0.40

$$E_{bY-Vac} = E_{fY-Vac} - E_{fY} - E_{fVac} \quad (2a)$$

$$E_{fY-Vac} = E_{confY-Vac} - \frac{N-2}{N} E_{conf\,id} - E_{cohY} \quad (2b)$$

$$E_{fY} = E_{confY} - \frac{N-1}{N} E_{conf\,id} - E_{cohY} \quad (2c)$$

$$E_{fVac} = E_{confVac} - \frac{N-1}{N} E_{conf\,id} \quad (2d)$$

where N is the number of atoms in the supercell, $E_{conf\,id}$ the total energy of the calculated ideal configuration, E_{cohY} the cohesive energy of Y, E_{fY} and E_{fY-Vac} the formation energies of one and Y-Fe vacancy pair in the *fcc* Fe lattice, respectively, E_{confY} the total energy of the calculated supercell with one Y substitute, $E_{confY-Vac}$ the total energies of the calculated supercell with Y-Fe vacancy pair and E_{bY-Vac} the binding energy of this pair in γ-Fe lattice.

The results presented in Table 3.3.4.2 confirm aforementioned expectations. Relative displacement of Y atom in the 1-NN configurations is the most significant (1.25 Å) and the binding energy is the largest (1.67 eV). In the 2-NN configuration there is no bonding between the Y substitute and Fe vacancy and in the 3-NN and 4-NN configurations of this pair the binding energies are 0.30 eV and 0.40 eV, respectively.

SUMMARY

Series of large-scale first principles calculations on perfect γ-Fe lattice as well as that containing a single Fe atom vacancy, O impurity atom, one or two Y substitutional atom as well as Y-Fe vacancy pair have been performed. This allows us to determine the pair-wise energies necessary for further kinetic Monte Carlo simulations. Since the interstitial migration of O atom is significantly faster than yttrium self-diffusion, the slow transfer of the oversized Y substitute atoms is a rate-determining process in Y_2O_3 nanoparticles formation. Our preliminary LKMC results show that the dissolved Y atoms tend to precipitate in a form of particles coherent with the iron matrix. Currently, we have begun modelling of the vacancy-assisted yttrium diffusion.

4. EFDA FUSION TECHNOLOGY PROGRAMME

The fusion technology physics work has been performed in close co-operation with other EURATOM Associations, in particular with EURATOM-UKAEA, Culham, EURATOM- FZK, Karlsruhe, and EURATOM-FOM, Petten.

4.1. DETERMINATION OF TRITIUM AND ANALYSIS OF CARBON-BASED PLASMA-FACING COMPONENTS BEFORE AND AFTER THEIR DETRITIATION WITH DIFFERENT METHODS

Principal investigator: ***G.Kizane***

INTRODUCTION

Carbon is considered as a prospective plasma-facing material for the International Thermonuclear Experimental Reactor (ITER) owing to its following advantages. A low atomic number, Z, of C (Z=6) reduces the detrimental effects of impurities in the plasma. Because of the ability of carbon to withstand high heat flux and its favourable thermomechanical properties (carbon sublimes rather than melts during disruptions or edge localised modes), carbon tiles have been widely used for the first wall of the Join European Torus (JET) and are the candidate material for the lower vertical targets of the divertor plates of ITER. According to the present design of ITER, the use of beryllium on the main wall (700 m^2), carbon on the high flux areas (50 m^2) and tungsten on the lower flux areas (100 m^2) of the divertor are foreseen. The erosion of the carbon of the first wall by D-T plasmas leads to a codeposition of hydrogenated carbon films mainly on the colder parts of the surfaces of the plasma chamber because of a high affinity of carbon to hydrogen isotopes. This immobilises substantial amount of tritium (up to 1 atom of tritium to 1 atom of carbon) in thin layers that are not accessible to further erosion. The formation of such co-deposited tritiated layers constitutes a major issue for ITER as it will tend to increase the tritium inventory trapped inside the fusion machine. Due to the maximum tritium inventory allowed inside the ITER machine, removal of trapped tritium will be regularly necessary to continue operation. Beryllium is also subjected to significant erosion under plasma-operating conditions; therefore a mixed Be-C film may form. Tritium depth profiles reported in literature for JET divertor carbon fibre composite (CFC) tiles revealed that a large fraction of the total tritium retained by a tile >61% had diffused deep into the bulk of the tile. For the reasons of safe operation of a fusion machine and safe disposal

of the used first-wall materials (FWM), the tritium retention and recovery from FWM require further investigations. The coring/full combustion technique is for the most part used in literature for determination of tritium depth profiles. Analysis of selected samples of plasma-facing components (PFCs) in order to support particle transport studies and development of in-situ detritiation methods has been proposed as the JET Fusion Technology activities in the frame of the EFDA 2008 Workprogramme. Investigations of properties of the tritium trapped in the deposited films, in the surface layers and in the bulk of CFC tiles with respect to temperature, radiation and magnetic field can contribute to the development of detritiation methods.

EXPERIMENTAL METHODS AND TECHNIQUES

PREPARATION OF SAMPLES FOR TRITIUM ANALYSIS

Samples for tritium analysis were prepared by core-drilling of tiles with a hollow drill of the diameter 10 mm and the cutting path of 1 mm in width. Then the cylinders obtained were cut into discs of 0.8 mm thickness using a diamond-grinding disc with a cutting path of 1 mm in width. The workplace for mechanical treatment of carbon-based tiles used for this study is shown in Fig. 4.1.1. Core drilling positions of tile 14BWG4B for tritium analysis in a poloidal direction is shown in Fig. 4.1.2. A cylinder and discs cut are shown in Fig. 4.1.3.

Figure 4.1.1. Workplace for mechanical treatment of carbon-based tiles

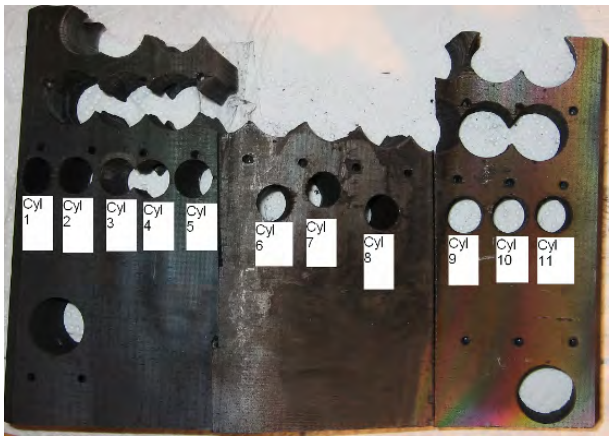

Figure 4.1.2. Core drilling positions of tile 14 BWG4B

a) b)

Figure. 4.1.3. Cylinder 1 (a) and discs 1-3 of cylinder 1 (b) of tile 14BWG4B.

COMBUSTION OF SAMPLES FOR TRITIUM ANALYSIS

In order to determine the tritium content in the carbon samples, we use the combustion technique proposed by Vance et all and employed in study JET-P(99)53. Two sets of the glassware of this apparatus were received from JET and one set of this apparatus was made by ourselves at the University of Latvia. Each of these 3 apparatuses was equipped with the necessary hardware for its operation – with a tube furnace of an appropriate size and a split hinge design, with a thermocouple (2 type S and 1 type K thermocouples are used for the 3 apparatuses), with a temperature control unit made by ourselves at the University of Latvia (3 temperature control units were made for the 3 apparatuses). Thermo-emfs of the type S and K thermocouples are measured with an Agilent 34970A multichannel digital voltmeter with an Agilent 34902A multiplexer and recorded with a personal computer (PC) using the Agilent-BenchLink Data-Logger 3 software. The temperatures of the cold junctions of the type S thermocouples were measured with type J thermocouples connected

directly to the Agilent 34902A multiplexer. A carbon-based disc for combustion is placed into a quartz crucible above the CuO wire bed in the quartz tube of the Vance apparatus (Fig.4.1.4.). A fume hood was set up and connected to a ventilation system for safe operation of 3 Vance apparatuses (Fig. 4.1.5). A new blower was purchased in order to increase a draught.

The combustion was normally performed under the conditions given in Table 4.1.1. The tritium was collected in two bubblers (Fig.4.1.4); 98-99 % of tritium was collected in the first bubbler. The time of a complete combustion, 4-6 h, depends on thickness of the carbon-based disc being combusted.

Table 4.1.1. Conditions of combustion of carbon-based samples

Combustion temperature, °C:	860
Flow rate of moistened air, mL/min:	15-20
Time of a complete combustion, h:	4-6
Cleaning time of the system, h:	15-20 (overnight)
Volume of distilled water in the 1st bubbler, mL:	200
Volume of distilled water in the 2nd bubbler, mL:	100

After each combustion 5 mL water aliquots were taken from each of the two bubblers. Each of these aliquots was mixed with 15 mL of an Ultima Gold scintillation cocktail and analysed for total tritium with a TRi-Carb 2910TR counter. Measuring time was 30 min in each of 3 cycles.

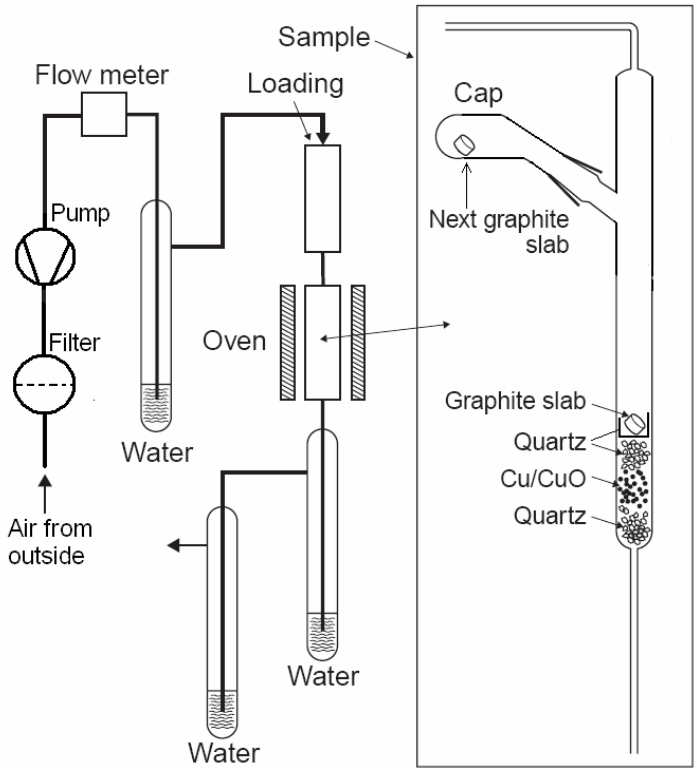

Figure 4.1.4. Scheme of a modified Vance apparatus for the combustion of carbon samples (adapted from report JET-P(99)53)

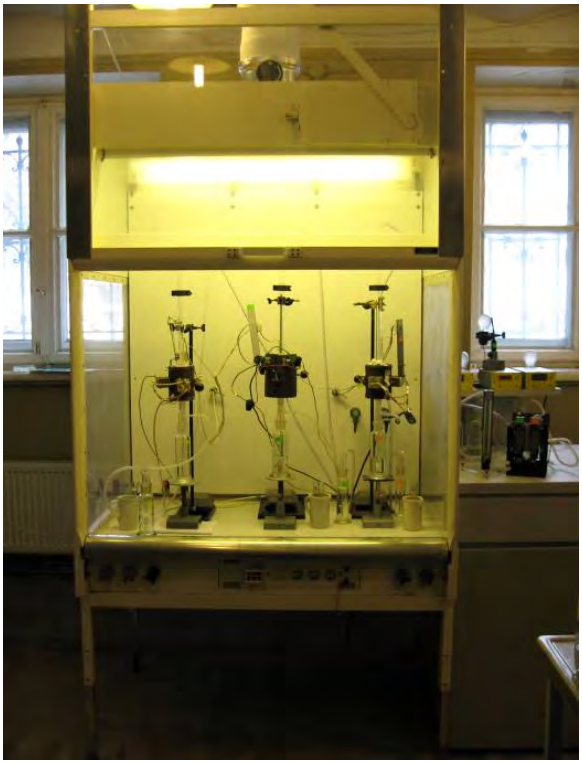

Figure 4.1.5. General view of fume hood with set-up of 3 Vance apparatuses

THERMAL DESORPTION OF TRITIUM

An apparatus for investigations of thermal desorption of tritium up to 1100 °C was set up in a laboratory at the University of Latvia. The experimental set-up comprises a cylinder with purge gas He + 0.1% H_2 from AGA and a pressure regulator from Linde, a Cole-Parmer 150-mm brass flowmeter with a high-resolution valve, a quartz tube with a type S thermocouple of 300 mm in length and a compartment containing granulated zinc from Aldrich operated at 390-400 °C, and tritium monitor TEM 2100A with gas flow-through proportional detector DDH 32 from MAB. The quartz tube consists of two compartments: a sample compartment of a 22 mm outside diameter and 430 mm in length with an inner quartz tube for a type S thermocouple, and a zinc compartment of less than 17 mm outside diameter and 140 mm in length. The sample compartment of the quartz tube is heated from the outside with a “Nabertherm” RT 50-250/13 tube furnace controlled with a P 320 controller. The zinc compartment is heated from the outside with a tube furnace of an appropriate size and a split hinge design. The zinc bed converts tritiated water to molecular gaseous tritium (HT, DT, and traces of T_2). The temperature of the zinc bed is measured with a type K thermocouple. The cold junction of the type S thermocouple is measured with a type J thermocouple.

In normal operation, the flow rate of purge gas He + 0.1% H_2 is 15 L/h, the sample temperature is initially increased linearly with time at the rate β=5 °C/min up to an end temperature of max. 1100 °C, which is kept constant for a pre-determined time (e.g. for 1 h).

The purge gas flow rate is controlled and recorded manually. The temperatures of the sample (thermo-emfs of the type S and J thermocouples) and the Zn bed (thermo-emf of the type K thermocouples) are continuously measured with an Agilent 34970A multichannel digital voltmeter with an Agilent 34902A multiplexer and recorded with a PC using the Agilent-BenchLink Data-Logger 3 software. The tritium activity in the purge gas, which is derived from the count rate of proportional counter DDH 32, is continuously measured with tritium monitor TEM 2100A at the counting time of 120 s and registered with a PC using an RS-232 serial printer interface of TEM 2100A. The count rate is corrected for the system background as determined at the start and the end of each experiment. The tritium release rate of the sample is calculated from the corrected count rate and the measured flow rate of the purge gas He + 0.1% H_2. The total released tritium activity is calculated by integrating the release rate over the time region where a release is measurable.

RESULTS AND DISCUSSION

RESULTS FROM TG AND DTA ANALYSIS

In order to check conditions for the combustion of carbon-based samples, thermogravimetric experiments were carried out under laboratory air from 27 °C to 1002 °C at the rate of temperature increase of 5 °C/min using a Seiko Exstar 6300 apparatus (Fig. 4.1.6). It is evident from curves in Fig. 4.1.6 that the combustion reaction reaches its maximum rate at 803-808 °C. Therefore a temperature of 850 °C is a reasonable choice for the temperature of the combustion of carbon-based samples in a Vance apparatus.

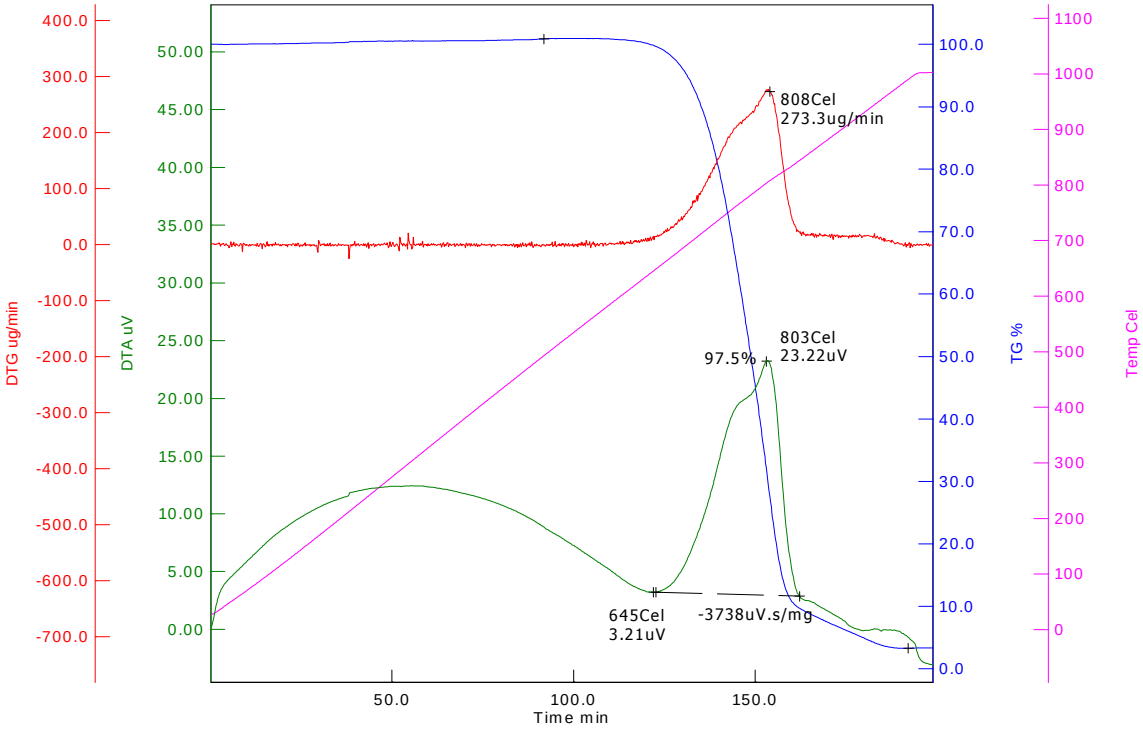

Figure 4.1.6. Thermogravimetric (TG), differential thermogravimetric (DTG), differential thermal analytic (DTA) curves of a CfC sample of 5.991 mg in air

DETERMINATION OF TOTAL TRITIUM IN CARBON-BASED DISCS BY FULL COMBUSTION

Distribution of tritium activity in cylinder 11 of tile 3BWG4A of total thickness of 36.2 mm is shown in logarithmic scale in Fig. 4.1.7. Carbon-based tile 3BWG4A has been taken out of the MkII Gas Box divertor of the JET, operated during the years 1998-2001. This cylinder was core drilled out of the tile and cut into discs in the Tritium Laboratory Karlsruhe. These discs were analyzed on tritium activity in our laboratory at the University of Latvia.

99.9% of tritium is located in the first disc A1 of cylinder 11 of tile 3BWG4A, the mass activity of the plasma-facing surface disc A1 was 0.6 GBq/g, but that of the next disc A2 was 0.17 MBq/g, for disc A3 – 96 kBq/g. Then the tritium activity gradually increases in the sequence of discs A3 to A17 and finally to the rest of the cylinder, i.e. for disc A17 – 0.17 MBq/g and for the rest – 0.32 MBq/g. The mass activity of tritium in linear scale for discs A2-A17 and the rest of cylinder 11 of tile 3BWG4A are shown in Fig. 4.1.8.

Residual ash was observed after combustion of the first disc A1 of cylinder 11 of tile 3BWG4A, but its weight was very little – below the weighing error (<0.00006 g).

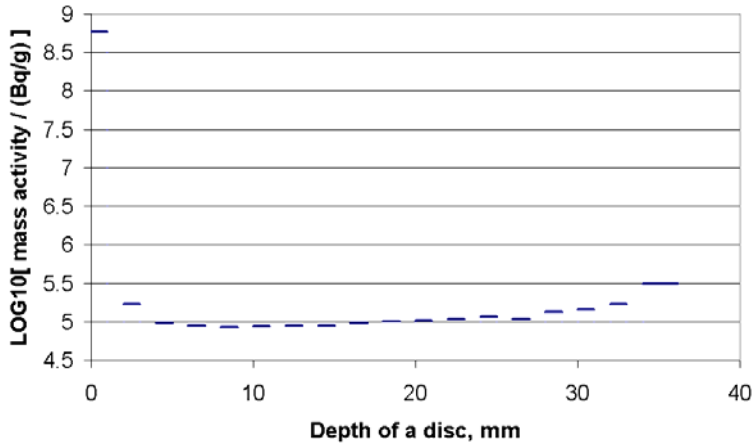

Figure 4.1.7. Distribution of tritium activity in cylinder 11 of tile 3BWG4A

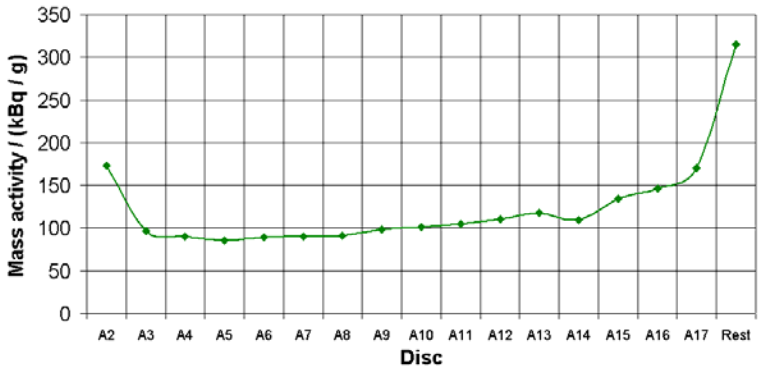

Figure 4.1.8. Mass activity of tritium for discs A2-A17 and the rest of cylinder 11 of tile 3BWG4A

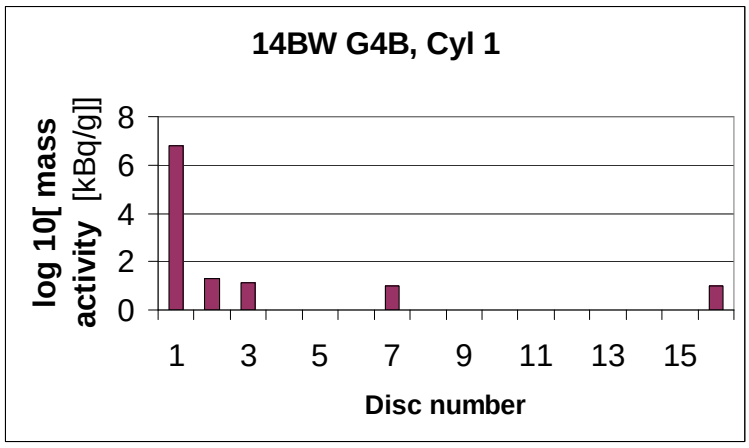

Figure 4.1.9. Distribution of tritium in cylinder 1 of tile 14BWG4B

Discs of cylinder 1 core-drilled out of the tile 14BWG4A were analysed. Most of tritium was detected in the first and second discs – A1 6.41 MBq/g and A2 20.03 kBq/g respectively. Tritium activities for discs A3, A7 and A16 were found to be approximately equal to 10 kBq/g. Distribution of tritium in cylinder 1 of tile 14BWG4B is shown in Fig. 4.1.9.

X-RAY DIFFRACTION ANALYSIS

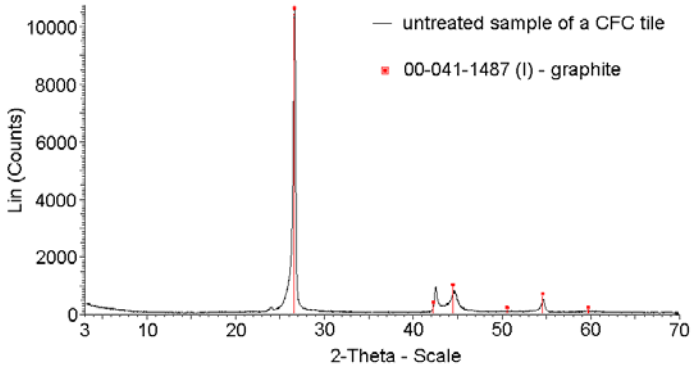

Figure 4.1.10X-ray diffraction pattern of untreated CFC tile 10057 G2

X-ray diffractometer (XRD) Bruker D8 Advanced was used for phase analysis of untreated CFC tile 10057 G2 (Fig. 4.1.10.). The X-ray diffraction pattern reveals only presence of graphite.

SURFACE ANALYSIS BY SCANNING ELECTRON MICROSCOPY (SEM)

SEM – EDAX Hitachi S-4800 and JSM 6490 was used for analysis of surface structure. Scanning electron micrographs of a disc from untreated CFC tile 10057 G2 are shown in Fig. 4.1.11. The micrographs show fibred structure of the CFC tile. Two types of fibres of different size - fine and coarse - are visible. Orientations of the fibres are different. Fine particles are observed on

the surface of coarse fibres. Diameter of fine fibres can be estimated as 7-11 µm, diameter of coarse fibres – about 50 - 55 µm.

Scanning electron micrographs of a disc from an inner part of CFC tile 3BW G4A are shown in Fig. 4.1.12. Fig. 4.1.12.a shows coarse fibres of different orientations. Interfibre porosity is visible. Fibre diameter can be estimated to be about 40 µm. A view of a separate coarse fibre is shown in Fig. 4.1.12.b. A multilayered concentric structure of the fibre around a core of diameter about 7-10 µm is visible.

a) 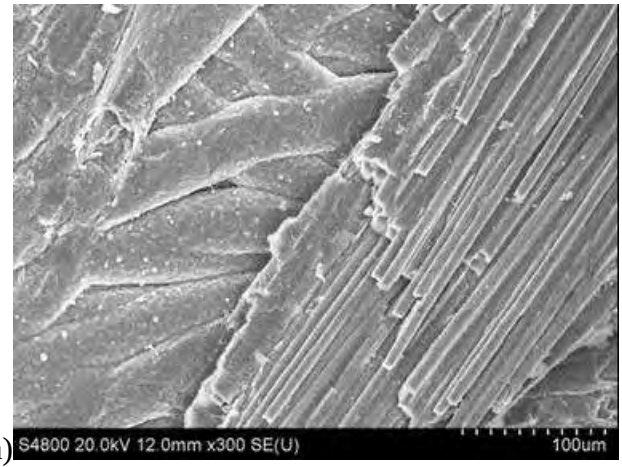

b) 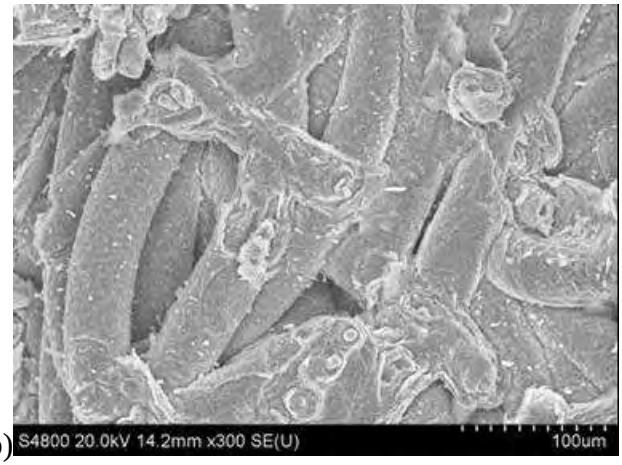

c) 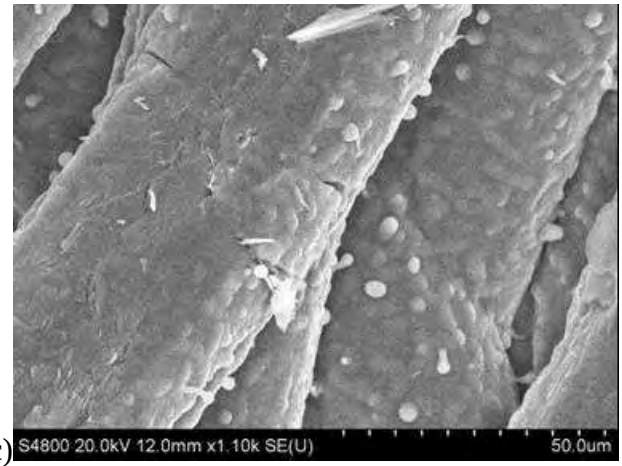

Figure 4.1.11. Scanning electron micrographs of a disc from untreated CFC tile 10057 G2

a) b)

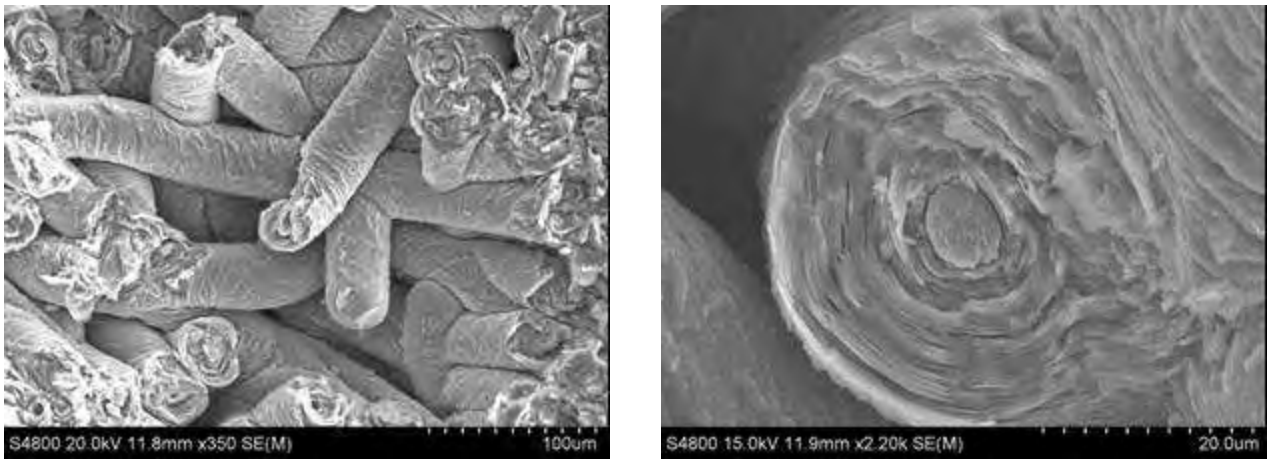

Figure 4.1.12. Scanning electron micrographs of a disc from an inner part of CFC tile 3BW G4A

TRITIUM RELEASE BY THERMAL DESORPTION

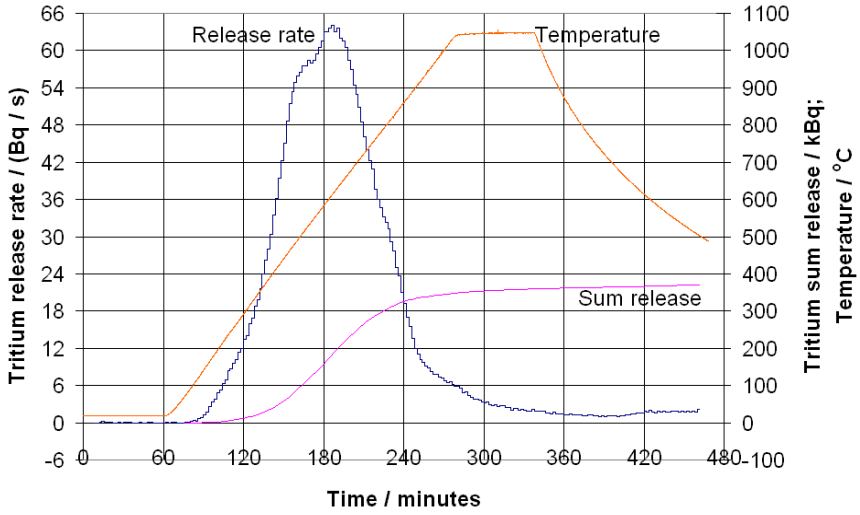

Figure 4.1.13. Tritium release by thermal desorption from disc A1 of cylinder 4 of tile 14BWG4B

Curves of tritium release at annealing of disc A1 of cylinder 4 of tile 14BWG4B at a rate of 5 °C/min to 1050 °C in a flow of He + 0.1% H_2 at a rate of 15 L/h are shown in Fig 4.1.13. The tritium release started at 140 °C, and its rate reached a maximum at 620 °C. At the end of the experiment, the total release of tritium was 0.37 MBq (Fig 4.1.13.) corresponding to the mass activity of tritium of 2.7 MBq/g. In this experiment, tritium release took place at lower temperatures than those in the case of disc A1 from cylinder 5 from JET tile 004/2-20 (report JET-P(99)53, page 21).

CONCLUSIONS

1. 99.9 % of tritium is located in the first disc of cylinder in plasma exposed side of 3BWG4A tile, the mass activity of the plasma-facing surface disc A1 was 0.6 GBq/g.

2. The tritium activity gradually increases in the sequence of discs A3 to A17 and finally to the rest of the cylinder, i.e. for disc A17 – 0.17 MBq/g and for the rest – 0.32 MBq/g.

3. Amount of tritium in the cylinder 1 of tile 14BWG4B gradually decreased from 1st to 3rd disc and then remained constant.

4. X-ray diffraction analysis of untreated CFC tile 10057 G2 shows only graphite.

5. Carbon fibres of two different sizes were observed by SEM.

4.2. EFFECTS OF MAGNETIC FIELD, RADIATION AND TEMPERATURE ON TRITIUM RELEASE FROM THE EXOTIC 8-3/13 NEUTRON-IRRADIATED BERYLLIUM PEBBLES

Principal investigator: ***G.Kizane***

INTRODUCTION

Beryllium pebbles are considered as a neutron multiplier according to the reference concept of the helium-cooled pebble-bed (HCPB) blanket in the European Breeding Blanket Programme for the DEMO design. Tritium accumulation in beryllium pebbles as a result of neutron-induced transmutations is a significant technological, safety and waste handling issue of the HCPB blanket. Considerable tritium retention can affect the tritium breeding and cause an environmental hazard in emergency and problems with utilization of used beryllium. Under the real operating conditions of the HCPB, the multiplier Be pebbles will be subjected to action of a high temperature up to 920 K, intense fast neutron radiation of 2.4 MW m^{-2} (i.e. 10^{18} n m^{-2} s^{-1}), and a high magnetic field (MF) of 7-10 T. Tritium and helium release from neutron-irradiated beryllium pebbles at annealing was explored previously. The present study is a continuation of our previous investigations of radiation and magnetic field effects on tritium release from neutron-irradiated beryllium pebbles. In our previous investigations, we found that tritium release from the EXOTIC 8-3/13 Be pebbles proceeds in general at lower temperatures than that from the BERYLLIUM pebbles. In this study, we investigated effects of radiation and magnetic field on tritium release from the EXOTIC 8-3/13 Be pebbles at temperatures up to 770 K as well as we investigated chemical forms of tritium after treatment of EXOTIC 8-3/13 Be pebbles and started to analyse chemical forms of tritium in PBA Be pebbles received from NRG (Petten) in the year 2008.

EXPERIMENTAL METHODS AND TECHNIQUES

SAMPLES INVESTIGATED

The beryllium pebbles irradiated in the EXOTIC 8-3/13 and PBA (Pebble Bed Assembly) experiment were investigated in this study. The irradiation programme EXOTIC (EXtraction Of Tritium In Ceramics) and PBA was carried out in the High Flux Reactor (HFR) in Petten, the Netherlands. EXOTIC 8-3/13 pebbles of a diameter 0 1-0.2 mm have been manufactured by spraying molten beryllium in an inert atmosphere (inert gas atomization process, IGA) at Brush Wellman Inc. Their grain size is 40 to 200 μm. The main impurities are 3400 ppm BeO, 100 ppm Mg. The Be pebbles were irradiated for 449.8 days in the HFR at temperatures 800-900 K with a neutron fluence of 2.7×10^{25} n m^{-2} (E > 0.1 MeV) of a fast fission spectrum. The ^{4}He content of 285

appm and the ^{3}H content of 1.16 appm (i.e. 138 MBq·g^{-1}) at the end of the irradiation in the year 2000 were calculated on the basis of the irradiation history. The PBA pebbles of a diameter 0.9-1.1 mm were irradiated 294 full power days in the HFR.

TRITIUM RELEASE AT ANNEALING

Annealing of Be samples about 9-13 mg was performed in a continuous flow of the purge gas He + 0.1% H_2 of the rate 14-15 L/h without and in MF of 1.7 T and/or 5 MeV fast-electron radiation of the dose rate P=14 MGy·h^{-1} in a special rig. The MF of 1.7 T was applied by means of a water-cooled electromagnet with a direct current of 60-65 A. The electromagnet has the interpolar gap of 20 mm in width and the channel of 20 mm in diameter in one of the poles for electron beam. A linear electron accelerator ELU-4 was used as a source of electron beam. The accelerator emits 4 μs pulses of 5 MeV electrons at the frequency of 200 Hz. At the normal operation, the average current of electron beam in the interpolar space was 6.3 μA, which corresponds to the dose rate of 14 MGy·h^{-1} for uniform absorption in the material up to 2.55 g·cm^{-2}. In the case of simultaneous action of electron radiation and MF, interaction of electrons with MF was minimized by directing the electron beam along the magnetic field lines in the rig.

The tritium released was measured continuously with a gas flow-through proportional meter TEM 2102A with a detector DDH 32 of the operating volume 300 cm^{3}. In order to estimate a pure contribution of radiation in the tritium release, samples of Be pebbles were subjected only to the action of fast-electron irradiation for 3 h without any additional heating. Temperature of the Be pebbles in these irradiation experiments was found to be below 550 K. The tritium release under the electron radiation was compared with the tritium release at the temperature ramp of 5 K/min to 553 K, then at 553 ± 5 K for 3 h, then the heater was switched off, and the sample was left to cool in a flow of the purge gas. In the second type of annealing experiments, the temperature programme was 5 K/min to 770 K, then at 770 ± 5 K for 1 h, then the heater was switched off, and the sample was left to cool in a flow of the purge gas. In the case of application of electron radiation in these experiments, the electron radiation was switched on for 3 h within 45-230 s after the start of the temperature programme 5 K/min. In the case of application of MF, MF was switched on before the start of the experiment and switched off, when the sample cooled below 370 K. The radioactivity of tritium released was calculated as MBq·g^{-1} to 1 g of the sample of Be pebbles.

LYOMETHOD OF TRITIUM ANALYSIS

In order to determine the total tritium activity and abundance ratios of chemical forms of tritium (T_2, T^0, T^+) in irradiated beryllium pebbles, two weighed amounts about 2-4 mg of the pebbles were dissolved in pure 2 mol/L H_2SO_4 and in a solution of 2 mol/L H_2SO_4 + 0.5-1 mol/L $Na_2Cr_2O_7$ in a special setup. At the dissolution in pure acid, the T_2 and T^0 localized in the Be pebbles transfer as T_2+HT into a gas phase, its rate of release was measured continuously with a meter TEM 2100A with a detector DDH 32. T^+ localized in a Be layer remains in the solution. After the Be pebbles had completely dissolved, the tritium activity in the solution was measured with a liquid scintillation method. The total tritium activity in the pebbles is a sum of the tritium in the gas phase and in the solution. In order to determine the chemical forms T^0 and T_2 separately, dissolution experiments with the scavenger of H^0 (T^0) – 0.5-1 mol/L $Na_2Cr_2O_7$ were performed.

RESULTS

TRITIUM RELEASE AT TEMPERATURES ≤553 K

Tritium release from the EXOTIC 8-3/13 Be pebbles at the temperature ramp of 5 K/min to 553 K and then at 553 K for 3 h both without and in MF of 1.7 T is shown in Fig. 4.2.1.a. Under the given conditions, tritium was released in a single broad peak starting with a steep increase at 410 K, reaching its maximum at 480-553 K, and then declining like an exponent towards a background level. The samples of the pebbles were found to be dissimilar with respect to the initial total tritium activity 2.5-4.5 MBq·g^{-1} and to the tritium fractional sum release at the annealing 10% - 19% (Fig. 4.2.1.a). The initial total tritium activity in MBq·g^{-1} was calculated to 1 g of the sample of Be pebbles as the sum of the activity of tritium released under the given temperature and/or irradiation programme and the total activity of tritium remained in the pebbles determined by dissolving them in pure 2 mol/L H_2SO_4.

Tritium release from the EXOTIC 8-3/13 Be pebbles under the action of electron radiation of 14 MGy·h^{-1} for 3 h without any additional heating and without MF is shown in Fig. 4.2.1.b. The electron radiation was switched on at the experiment time 30 min and switched off at the time 210 min. Temperature given in the curves in Fig. 4.2.1.b is the temperature of the sample measured with a thermocouple of type S. The thermocouple was located beneath the sample and was not within a direct electron beam. According to the temperature curves in Fig. 4.2.1.b, the sample temperature increased rapidly to 440-478 K within 10 min after switching the electron radiation on, then the temperature was in a range 420-550 K. Under the electron radiation, tritium was released in a single comparatively narrow peak starting with a steep increase shortly after the switching on of the electron radiation, reaching its maximum at <500 K, and then declining like an exponent towards a

background level. The initial total tritium activity of the pebble samples was 2.6-4.6 MBq·g^{-1}, and the tritium fractional sum release was 17% - 26% (Fig. 4.2.1.b).

Tritium release from the EXOTIC 8-3/13 Be pebbles under the simultaneous action of electron radiation of 14 MGy·h^{-1} for 3 h and MF of 1.7 T without any additional heating is shown in Fig. 4.2.1.c. The shape of the tritium release curves is qualitatively similar to that in Fig. 4.2.1.b. The samples investigated in this series were comparatively similar with respect to their initial total tritium activity 4.7-5.3 MBq·g^{-1}. The tritium fractional sum release from these samples was 21% - 29% (Fig. 4.2.1.c).

It is worth noting that the dissimilarity of the batch of the EXOTIC 8-3/13 Be pebbles investigated may be characterized by the fact that the batch contained also some coarse agglomerates of the pebbles containing 10-19 MBq·g^{-1} of tritium, having also a high tritium fractional sum release about 50% at annealing at 553 K for 3 h without radiation and without MF.

TRITIUM RELEASE AT TEMPERATURE 770 K

Tritium release from the EXOTIC 8-3/13 Be pebbles at the temperature ramp of 5 K/min to 770 K and then at 770 K for 1 h both without and in MF of 1.7 T is shown in Fig. 4.2.2.a. Two distinct peaks are evident on the curves of the tritium release rate in Fig. 4.2.2.a. The peak temperatures are summarized in Table 4.2.1. The initial total tritium activity of the pebble samples was found to be 3.6-5.3 MBq·g^{-1}, and the values of the tritium fractional sum release are 17% - 24% without MF (curves 1 and 2, Fig. 4.2.2.a) and 25% in MF of 1.7 T (curve 3, Fig. 4.2.2.a).

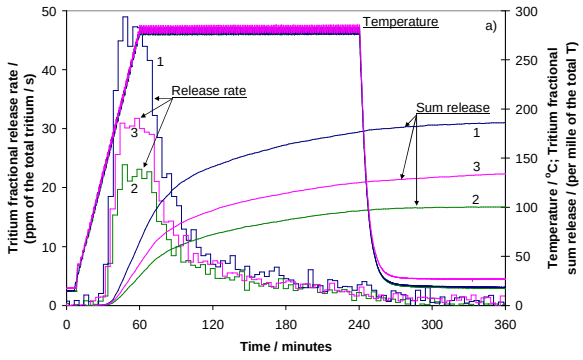

a)

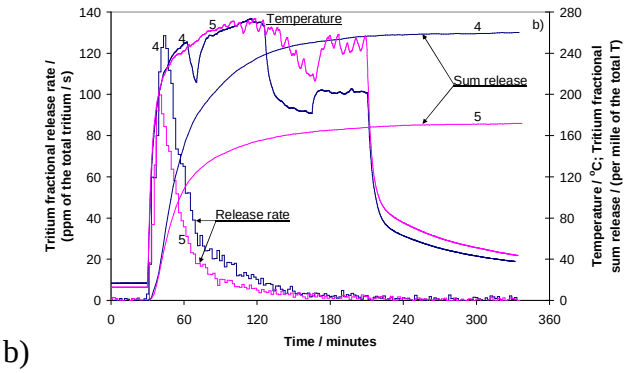

b)

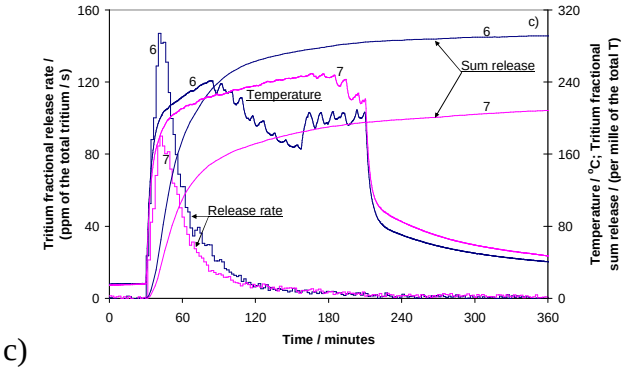

c)

Figure. 4.2.1. Tritium release at annealing of samples of the EXOTIC 8-3/13 Be pebbles in a continuous flow of 14-15 L/h of He + 0.1 % H_2 under the following conditions: a) – at the given temperature programme without MF (1, 2) and in MF of 1.7 T (3); b) – the action of electron radiation of 14 MGy·h^{-1} for 3 h without additional heating and without MF; c) – the simultaneous action of electron radiation of 14 MGy·h^{-1} for 3 h and MF of 1.7 T without additional heating. The curves of the tritium fractional release have been calculated for the following values of the initial total tritium activity for 1 g of the sample, MBq·g^{-1}: 1 – 2.52; 2 – 4.50; 3 – 4.06; 4 – 2.62; 5 – 4.56; 6 – 5.31; 7 – 4.67

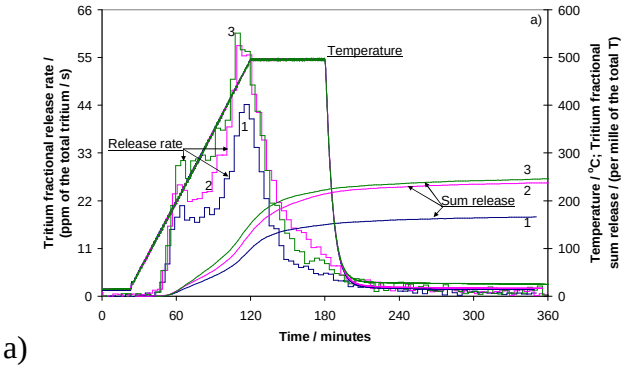

a)

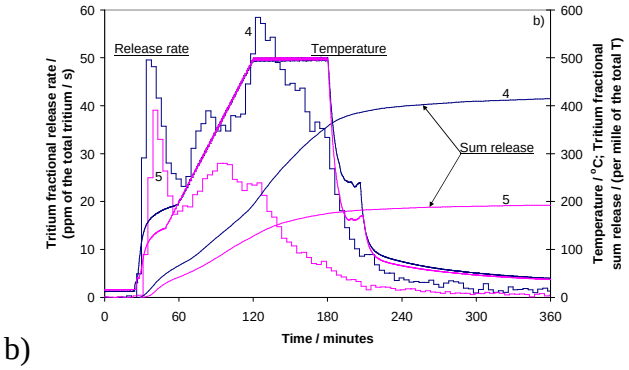

b)

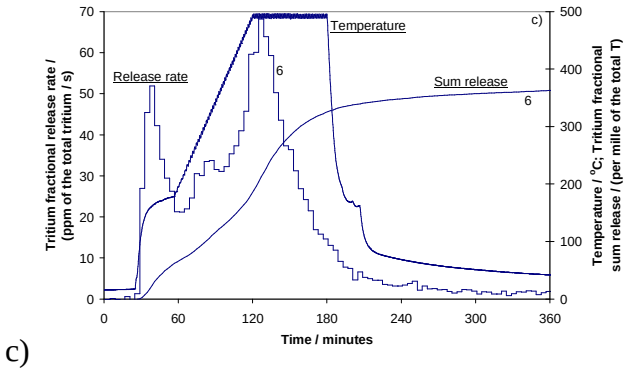

c)

Figure 4.2.2. Tritium release at annealing of samples of the EXOTIC 8-3/13 Be pebbles in a continuous flow of 14-15 L/h of He + 0.1 % H_2 under the following conditions: a) – at the given temperature programme without MF (1, 2) and in MF of 1.7 T (3); b) – at the given temperature programme under the action of electron radiation of 14 MGy·h^{-1} for 3 h without MF; c) – at the given temperature programme under the simultaneous action of electron radiation of 14 MGy·h^{-1} for 3 h and MF of 1.7 T. The curves of the tritium fractional release have been calculated for the following values of the initial total tritium activity for 1 g of the sample, MBq·g^{-1}: 1 – 5.34; 2 – 4.31; 3 – 3.62; 4 – 5.23; 5 – 8.61; 6 – 5.84

Table 4.2.1. Temperatures of the peak values of the tritium release rate in Fig. 4.2.2a.

Curve no. in Fig. 4.2.2.a.	MF, T	Temperature of the minor peak, K	Temperature of the maximum peak, K
1	0	485-496	753-764
Not shown	1.7	490-505	725-734
2	0	484-495	724-733
3	1.7	484-499	718-727

Tritium release from the EXOTIC 8-3/13 Be pebbles under the action of electron radiation of 14 MGy·h^{-1} for 3 h and the temperature programme but without MF is shown in Fig. 4.2.2.b. The

first peak in the curves of the tritium release rate is at the temperature below 470 K. At the first maximum, i.e. at the time 60 min, 4.2% - 6.6% of the initial total tritium activity was released (Fig. 4.2.2.b). Evidently, that this maximum is caused mostly by the electron radiation as there is no maximum of this kind at the temperature <470 K in the tritium release curves of the experiments without electron radiation. The second peak is a broad peak at the temperature >470 K, corresponding to the simultaneous action of temperature >470 K and radiation. Patterns of the tritium release were found to be highly dissimilar for the four samples of the EXOTIC 8-3/13 Be pebbles investigated in this series of experiments. The initial total tritium activity of the pebble samples investigated in these experiments was 4.9-8.6 $MBq \cdot g^{-1}$, and the values of the tritium fractional sum release were found to be in the range 19% - 71%. The tritium release curves given in Fig. 4.2.2.b illustrate this dissimilarity.

Tritium release from the EXOTIC 8-3/13 Be pebbles under the simultaneous action of electron radiation of 14 $MGy \cdot h^{-1}$ for 3 h, the temperature programme and MF of 1.7 T is shown in Fig. 4.2.2.c. Similarly to the curves in Fig. 4.2.2.b, the two distinct peaks are present in the curve of the tritium release rate given in Fig. 4.2.2.c. At the first maximum at the temperature <470 K, i.e. at the time 60 min, 6.6% - 7.6% of the initial total tritium activity was released (Fig. 4.2.2.c). The initial total tritium activity of the pebble samples investigated in these experiments was 4.0-5.8 $MBq \cdot g^{-1}$, and the values of the tritium fractional sum release were found to be in the range 32% - 37% (Fig. 4.2.2.c).

CHEMICAL FORMS OF TRITIUM IN THE BE PEBBLES

The abundance ratios of the separate chemical forms in the pebbles change after tritium release at annealing the pebbles under action of radiation and magnetic field separately and simultaneously.

In the presence of radiation and magnetic field, at annealing of the EXOTIC 8-3/13 pebbles at relatively low temperature 553 K for 3 h, 20-29 % of the localised tritium was released, in the presence of ionizing radiation of fast electrons, up to 20 % of tritium was released, but at temperature only 10-15%. After such treatment in the presence of magnetic field and radiation, the abundances of the chemical forms of the residual tritium had the following values - the amount of molecular tritium in the pebbles decreased to 30-35 %, the atomic tritium to 20-30 %, but the amount of tritium in the ionic form did not change in comparison with an initial amount of tritium. At such a low thermo-annealing temperature 553K, the amount of residual molecular tritium did not change, and only release of atomic tritium was observed. In the case of annealing under action of radiation (R, T), we can conclude that the fast electron radiation in experiments cause radiolysis of a

fraction of T_2 in bubbles ($T_2 \rightarrow T^o + T^o$), but temperature is too low for larger release of tritium. In the case of annealing under action of all the three factors simultaneously (R, MF, T), residual amount of molecular tritium reduces much more because the magnetic field can cause spin transformation (S→T) in the pairs of radicals generated by radiolysis; the efficiency of recombination of atomic tritium decreases, and diffusion of tritium in form of atomic tritium T^o increases.

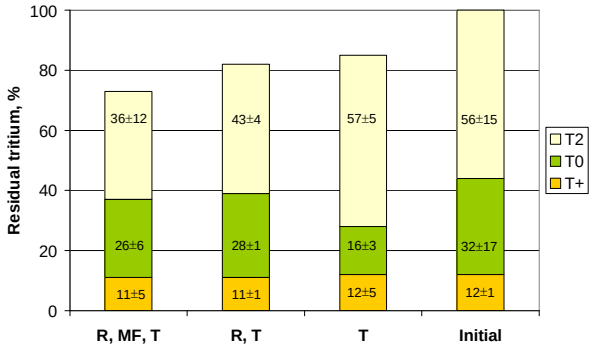

Figure. 4.2.3. Chemical forms of tritium in EXOTIC 8-3/13 beryllium pebbles after the treatments: R, MF, T – radiation, magnetic field and temperature; R, T – radiation and temperature; T – temperature only; initial – the pebbles without treatment. Radiation – accelerated 5 MeV electrons, 14 MGy·h^{-1}; MF – 1.7 T, temperature 553 K, time – 3 h.

Annealing the EXOTIC 8-3/13 pebbles at a higher temperature 770 K for 1 h, 17 – 24 % of localized tritium was released into the gaseous phase. The abundance ratios of the chemical forms of the residual tritium change to the following values – the molecular tritium – 30-55 %, atomic – 40-45 %, ionic form – 10-14 %. At annealing EXOTIC 8-3/13 pebbles at 770 K in the simultaneous presence of magnetic field and radiation, the abundances of the chemical forms of the residual tritium changes with the same trend as at 553 K – the amount of molecular tritium in the pebbles decreases considerably down to 30-40 %, the atomic tritium decreases to 20 - 30 %, but the tritium in the ionic form does not change substantially. The changes in the chemical forms as a result of the treatments of EXOTIC 8-3/13 pebbles are larger than those of BERYLLIUM pebbles determined in the previous investigations.

The main form of tritium in the PBA Be pebbles is molecular tritium T_2. Untreated PBA Be pebbles contain molecular tritium T_2 – 90-95 %, atomic tritium – 2 - 5 % and ionic form of tritium T^+ – 2-5 %, the activity of tritium in 1 gram of PBA Be pebbles is 2-4 GBq/g.

DISCUSSION

It is worth noting that, similarly as in, an appreciable fraction of tritium is released at temperatures lower than the irradiation temperature 800-900 K. A minor peak at 550 K, where the tritium release rate is about by a factor of 4 lower than that in the largest peak at 1173 K, was

observed at a constant heating rate of 7 K/min in. The reason of this phenomenon could be the fact that at the EXOTIC neutron irradiation the rate of tritium production is higher than the rate of tritium release and some post irradiation relaxation of structure could take place.

The data on the initial total tritium activity and the tritium fractional release given in Figs. 4.2.1 and 4.2.2 are summarized in Fig. 4.2.4. The samples of the EXOTIC 8-3/13 Be pebbles investigated were found to be dissimilar with respect to these parameters. Likewise to BERYLLIUM pebbles, the dissimilarity of the EXOTIC 8-3/13 Be pebbles could be explained by the different contents of tritium and impurities in Be pebbles caused by different temperatures and neutron fluxes of separate pebbles and also by differing pebble microstructures. The total tritium activity of our samples of the EXOTIC 8-3/13 Be pebbles was found to be 2.5-19 MBq$\cdot$g^{-1}, which is many times lower than the tritium activity 88 MBq$\cdot$g^{-1} in the year 2008, corresponding to 138 MBq$\cdot$g^{-1} calculated on the basis of the irradiation history for the year 2000.

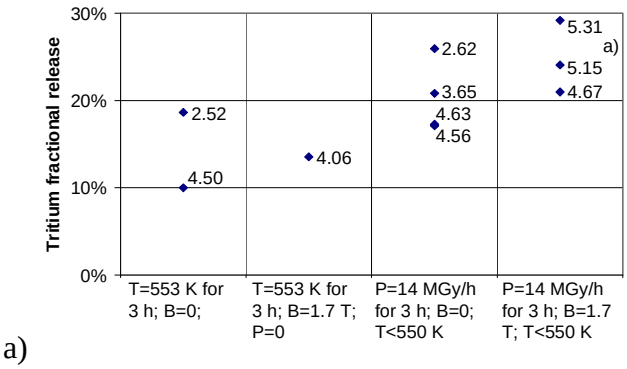

a)

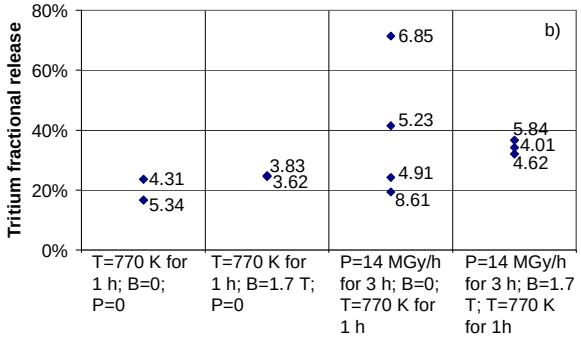

b)

Figure 4.2.4. Values of the fractional release of tritium from the samples of the EXOTIC 8-3/13 Be pebbles having the initial total tritium activity 2.5-5.3 MBq$\cdot$g^{-1} (a) and 3.6-8.6 MBq$\cdot$g^{-1} (b) at the temperature ≤553 K for 3 h (a) and 770 K for 1 h (b) without or with electron radiation of P=14 MGy$\cdot$h^{-1} for 3 h and without or with MF of 1.7 T. Values of the initial total tritium activity (MBq$\cdot$g^{-1}) are given as labels to the data points

Nevertheless, we can conclude a trend that the electron radiation causes a higher fractional release of tritium than a simple thermal treatment of a longer duration and a higher temperature (Fig. 4.2.4.a) or a similar temperature programme without the electron radiation (Fig. 4.2.4.b), and a trend that at a given temperature programme the simultaneous action of the electron radiation and MF of 1.7 T causes a higher fractional release of tritium than a similar electron radiation of the same duration but without MF. A similar trend was observed for the tritium release from neutron-irradiated beryllium pebbles and for the detritiation of D-T-plasma-exposed beryllium tiles from JET.

At the tritium release at annealing the pebbles under action of radiation and magnetic field separately and simultaneously, the abundance ratios of separate chemical forms in the pebbles change. It is related to radiolysis of localized T_2 into pairs of radicals of T^0 and MF-induced spin transformation S→T in pairs of radicals resulting in an increase of concentration of T^0 – main diffusing particles in beryllium metal.

CONCLUSIONS

1. The samples of the EXOTIC 8-3/13 Be pebbles investigated were found to be dissimilar with respect to the initial total tritium activity and the tritium fractional release under the given conditions.

2. A trend that the electron radiation causes a higher fractional release of tritium than the same temperature programme without the electron radiation was observed.

3. A trend that the simultaneous action of the electron radiation, the temperature programme and magnetic field of 1.7 T causes a higher fractional release of tritium than the simultaneous action of the electron radiation, the temperature programme but without magnetic field can be concluded.

4. At annealing EXOTIC 8-3/13 pebbles at 770 K and at 553 K in the simultaneous presence of magnetic field and radiation, the abundances of the chemical forms of the residual tritium changes, but the tritium in the ionic form does not change substantially. The changes in the chemical forms as a result of the treatments of EXOTIC 8-3/13 pebbles are larger than those of BERYLLIUM pebbles determined in the previous investigations.

5. The main form of tritium in the PBA pebbles is molecular tritium T_2. Its abundance ratio (90-95 %) is larger than that of the beryllium pebbles from the BERYLLIUM (85-94 %) and EXOTIC 8-3/13 (41-71 %) irradiation experiments.

5. STAFF MOBILITY ACTIONS

5.1. STAFF MOBILITY VISITS

Olgerts Dumbrajs	worked at IPP Garching from 1st October until 30th November
Aleksejs Gopejenko	worked at Forschungszentrum Karlsruhe from 19th May until 18th June
Gunta Kizane	took part in the Task Force PWI 2008 Annual Meeting, JET, Culham, from 21st until 24th July, in the Workshop on PIE of HIDOBE irradiation programme, NRG, Petten from 18th until 21st August, and in the Kick-off Meeting "EUROBREED" FZK, Karlsruhe from 1st until 5th November
Aigars Vitins	took part in the Task Force Fusion Technology General Meeting, JET, Culham from 22nd until 25th April, and in the 7th Annual Meeting of the EU-PWI Task Force, ENEA, Frascati from 28th October until 1st November
Yurijs Zhukovskis	worked at Forschungszentrum Karlsruhe from 15th until 22nd March and from 5th until 18th October.
Guntars Zvejnieks	took part in the ITM Euratom Meeting, Frascati and Portici from 9th until 19th September, 2008.

6. OTHER ACTIVITIES

6.1. CONFERENCES, WORKSHOPS AND MEETINGS

Olgerts Dumbrajs took part in the Solvey workshop dedicated to memory of Radu Balescu, Brussels, 6 - 8 March, Belgium, in the IEEE International Conference on Plasma Science, Karlsruhe, Germany, June 15 - 19, in the 7th International Workshop "Strong Microwaves: Sources and Applications" July 27 – August 2, Nizhny Novgorod, Russia, and in the 33rd International Conference on Infrared, Millimeter, and Teraherz Waves, California, USA, September 15 - 19.

Aleksejs Gopejenko took part in the 24th ISSP scientific conference (Riga, Latvia, March, in the 6th International Conference "Information Technologies and Management", IT&M'2008 (Riga, Latvia, April, 2008), and in the 25th International Symposium on Fusion Technology, Rostock, Germany, September, 2008.

Gunta Kizane participated in the 24th Scientific Conference of the Institute of Solid State Physics of the University of Latvia, dedicated to commemoration of 30 years of the Institute of Solid State Physics (Riga, Latvia, February 20-22, 2008), in the International Baltic Sea Region Conference "Functional materials and nanotechnologies 2008 (FM&NT-2008)" (Riga, Latvia, April 1-4, 2008)

Aigars Vitins participated in the 25th Symposium on Fusion Technology, (SOFT-25), Rostock, Germany, September 13-21, 2008.

Maris Kundzins participated in the Public Information Group meeting, Lisbon, May 8-9, 2008.

6.2. VISITORS

Dr. Christian Grisolia, Dr. Joseph Paul Coad and Dr. Nicolas Bekris visited the Institute of Chemical Physics of the University of Latvia for the Kick-off meeting of task JW8-FT-1.12 on 28-30 January 2008.

6.3. VIDEO CONFERENCES

1. EU-HPC (High Performance Computing) meeting in Julich, February 13th, 2008.
2. EURATOM - University of Latvia Steering Committee Meeting in Riga, July 10th, 2008.
3. Lisbon – Frascati – Riga "Fusion Physic Discussion", December 15th, 2008.

6.4. TELEPHONE-CONFERENCES

1. Semi annual monitoring meeting I – JET Fusion Technology on the task JW8-1.12- the 12th June 2008.
2. Semi annual monitoring meeting II - JET Fusion Technology on the task JW8-1.12- the 4th December 2008.

7. PUBLICATIONS 2008

7.1 FUSION PHYSICS AND PLASMA ENGINEERING

7.1.1 PUBLICATIONS IN SCIENTIFIC JOURNALS

1. O.Dumbrajs, V.Igochine, and H.Zohm, *"Diffusion in a stochastic magnetic field in ASDEX Upgrade"*, Nucl. Fusion **48**, 024011 (2008).
2. D.Constantinescu, O.Dumbrajs, V.Igochine, and B.Weyssow, *"On the accuracy of some mapping techniques used to study the magnetic field dynamics in tokamaks,"* Nucl. Fusion **48**, 024017 (2008).
3. V.Igochine, O.Dumbrajs, and H.Zohm, *"Transition from quasiperiodicity to chaos just before sawtooth crash in the ASDEX Upgrade tokamak"* Nucl. Fusion **48**, 062001 (2008).
4. O. Dumbrajs, V. Igochine, and H. Zohm, *"Hysteresis in sawtooth crash in ASDEX Upgrade tokamak"*, The Open Plasma Physics Journal **1**, 9 (2008).
5. O.Dumbrajs and T.Idehara, *"Hysteresis in mode competition in high power 170 GHz gyrotron for ITER"* Int. J. Infrared Milimeter Waves **29**, 232 (2008).
6. Z.C.Ioannidis, O.Dumbrajs, and I.G.Tigelis, *"Linear and non-linear inserts for Genuinely wideband continuous frequency tunable coaxial gyrotron cavities,"* Int. J. Infrared Millimeter Waves **29**, 416 (2008).
7. Z.C.Ioannidis, G.P.Latsas, I.G.Tigelis, and O.Dumbrajs, *"TM Modes in Coaxial Cavities with Inner Surface Corrugations"* IEEE Trans. Plasma Sci. **36**, 2613 (2008).

8. J.Butikova and I.Tale, *"Laser-induced breakdown spectroscopy application for determining impurity content and depth profile in the plasma facing materials"* Journal of Nuclear Materials.

9. R.B.Gomes, H.Fernandes, C.Silva, A.Sarakovskis, T.Pereira, J.Figueiredo, B.Carvalho, A.Soares, P.Duarte, C.Varandas, O.Lielausis, A.Klyukin, E.Platacis, I.Tale and A.Alekseyv. "Liquid gallium jet–plasma interaction studies in ISTTOK tokamak" Journal of Nuclear Materials, 390-391 (2009) 938-941.

7.1.2 CONFERENCE ARTICLES

10. O.Dumbrajs, *"Stochastic processes in gyrotrons,"* Solvey workshop dedicated to memory of Radu Balescu, Brussels, 6 - 8 March, 2008, Belgium.

11. O.Dumbrajs and T. Idehara,*"Hysteresis in mode competition in high power 170 GHz gyrotron for ITER"* 2008 IEEE International Conference on Plasma Science, Karlsruhe, Germany, June 15 - 19, 2008.

12. O.Dumbrajs, M.Yu.Glyavin, T.Idehara, Z.C.Ioannidis, V.I.Khizhnyak, A.G.Luchinin, M.V.Morozkin, T.Saito, and I.G.Tigelis, *"Continuously tunable coaxial gyrotrons"*, 7th International Workshop "Strong Microwaves: Sources and Applications" July 27 – August 2, 2008, Nizhny Novgorod, Russia.

13. B. Piosczyk, S. Alberti, F. Albajar, K.Avramidis, P. Benin, T. Bonicelli, S. Cirant, O.Dumbrajs, D.Fasel, J.Flamm, G.Gantenbein, T.Goodman, J.-P.Hogge, S.Illy, S.Jawla, J.Jin, S.Kern, C.Lievin, I.Pagonakis, O.Prinz, T.Rzesnicki, M.Thumm, and M.Q.Tran *"Status of the European 2 MW, 170 GHz coaxial cavity gyrotron for ITER."* 7th International Workshop "Strong Microwaves: Sources and Applications" July 27 – August 2, 2008, Nizhny Novgorod, Russia.

14. O. Dumbrajs, Y.Kominis, and G.S.Nusinovich, *"Gyrotron dynamics in the process of mode switching in gyrotrons,"* 33rd International Conference on Infrared, Millimeter, and Teraherz Waves, California, USA, September 15 -19, 2008.

15. S.Kern, A.Avramides, M.H.Beringer, O.Dumbrajs, and Y.H.Liu, *"Gyrotron mode competition calculations: investigations on the choice of numerical parameters,"* 33rd International Conference on Infrared, Millimeter, and Teraherz Waves, California, USA, September 15 -19, 2008.

16. V.Igochine, O.Dumbrajs, H.Zohm,and ASDEX Upgrade team, *"Sawtooth crash as a result of quasiperiodic transition to chaos in ASDEX Upgrade,"* 35th European Physical Society Conference on Plasma Physics, June 9-13, 2008, Greece.

17. V.Igochine, O.Dumbrajs, H.Zohm, G.Papp, G.Por, G.Pokol, and ASDEX Upgrade team, *"The role of stochastization in fast MHD phenomena on ASDEX Upgrade,"* 22nd IAEA Fusion Energy Conference, 13-18 October 2008, Geneva, Switzerland.

18. A.Gopejenko, Yu.F.Zhukovskii, P.V.Vladimirov, and E.A.Kotomin, "*Ab initio* calculations of O and Y impurities in Fe *fcc* lattice". *24th ISSP scientific conference (Riga, Latvia, March, 2008).* Abstract: p. 4.

19. A.Gopejenko, Yu.F.Zhukovskii, P.V.Vladimirov, and E.A.Kotomin, "*Ab initio* calculations of oxygen and yttrium impurities in *fcc* Fe". *6th International Conference "Information Technologies and Management", IT&M'2008 (Riga, Latvia, April, 2008).* Abstracts: p. 23.

20. A.Gopejenko, Yu.F.Zhukovskii, P.V.Vladimirov, E.A.Kotomin, and A.Moslang, "Simulation of yttrium oxide particle formation in iron in support of ODS steel development". *25th International Symposium on Fusion Technology, (Rostock, Germany, September, 2008).* Abstracts: p. 226.

7.2 FUSION TECHNOLOGY

7.2.1 PUBLICATIONS IN SCIENTIFIC JOURNALS

21. Juris Tīliks, Gunta Ķizāne, Aigars Vītiņš, Elīna Kolodinska, Vija. Tīlika, Broņislavs Leščinskis. "Tritium sorption and desorption from JET beryllium tiles under temperature, electron radiation and magnetic field," Fusion Engineering and Design, **83**, 1388 (2008).

22. J.P.Coad, D.E.Hole, E.Kolodinska, J.Likonen, S.Lindig, G.F.Matthews, M.Mayer, V.Phillips, V.Riccardo, A.Widdowson and JET-EFDA Contributors. "Testing of tungsten coatings in JET for the ITER-like wall," Journal of Nuclear Materials (2009), doi:10.1016/j.jnucmat.2009.01.260 (in press).

23. J. Tīliks, G. Ķizāne, A. Vītiņš, E. Kolodinska, J.Tīliks Jr., I. Reinholds "Tritium release from beryllium articles for use in fusion devices," Journal of Nuclear Materials 386-388 (2009) 874-877.

24. Juris Tīliks, Aigars Vītiņš, Gunta Ķizāne, Vija Tīlika, Elīna Kolodinska, Sarmīte Kalēja, Broņislavs Leščinskis "Effects of external energetic factors on tritium release from the EXOTIC 8-3/13 neutron-irradiated beryllium pebbles," Fusion Engineering and Design (2009), doi:10.1016/j.fusengdes.2009.01.032 (in press).

7.2.2 CONFERENCE ARTICLES

25. J.Tīliks, V.Tīlika, G.Ķizāne, A.Vītiņš, A.Supe, A.Actiņš Fabrication of nanostructured lithium orthosilicate ceramic pebbles as tritium breeder material for thermonuclear reactors.” In the book: The Scientific Proceedings of Riga Technical University. Series “Material Science and Applied Chemistry”. 2008. Vol. 16. Pp. 17-20

26. J.Tiliks, G.Kizane, A.Vitins, E.Kolodinska, V.Tilika, S.Kaleja “Chemical forms of tritium in Be pebbles after different treatments.” – Preprints of the 22nd IAEA Fusion Energy Conference (IAEA FEC 2008) held in Geneva, Switzerland, October 13-18, 2008. Preprint FT/P2-14. – 5 p. Available online at: http://www.fec2008.ch/preprints/ft_p2-14.pdf